Design of a Microfluidic Device for the Analysis of Biofilm Behavior in a Microbial Fuel Cell

by

A-Andrew D. Jones, III

S.B., Department of Mathematics, Massachusetts Institute of
Technology (2010)
S.B., Department of Mechanical Engineering, Massachusetts Institute of
Technology (2010)

Submitted to the Department of Mechanical Engineering
in partial fulfillment of the requirements for the degree of

Masters of Science in Mechanical Engineering

at the

MASSACHUSETTS INSTITUTE OF TECHNOLOGY

February 2014

© Massachusetts Institute of Technology 2014. All rights reserved.

Author . . . .
Department of Mechanical Engineering
January 18, 2014

Certified by . . . .
Cullen R. Buie
Assistant Professor of Mechanical Engineering
Thesis Supervisor

Accepted by . . . .
David E. Hardt
Ralph E. and Eloise F. Cross Professor of Mechanical Engineering
Chairman, Department Committee on Graduate Theses

Design of a Microfluidic Device for the Analysis of Biofilm Behavior in a Microbial Fuel Cell

by

A-Andrew D. Jones, III

Submitted to the Department of Mechanical Engineering
on January 18, 2014, in partial fulfillment of the
requirements for the degree of
Masters of Science in Mechanical Engineering

Abstract

This thesis presents design, manufacturing, testing, and modeling of a laminar-flow microbial fuel cell. Novel means were developed to use graphite and other bulk-scale materials in a microscale device without loosing any properties of the bulk material. Micro-milling techniques were optimized for use on acrylic to achieve surface roughness averages as low as $R_a = 100\,\text{nm}$ for a $55\,\mu\text{m}$ deep cut. Power densities as high as $0.4\,\text{mW} \cdot \text{m}^{-2}$, ($28\,\text{mV}$ at open circuit) in the first ever polarization curve for a laminar-flow microbial fuel cell. A model was developed for biofilm behavior incorporating shear and pore pressure as mechanisms for biofilm loss. The model agrees with experimental observations on fluid flow through biofilms, biofilm structure, and other biofilm loss events.

Thesis Supervisor: Cullen R. Buie
Title: Assistant Professor of Mechanical Engineering

Acknowledgments

THIS PAGE INTENTIONALLY LEFT BLANK

Contents

List of Figures

List of Tables

THIS PAGE INTENTIONALLY LEFT BLANK

Chapter 1

Introduction

1.1 Fundamentals of biofilm dynamics

A biofilm is a community of bacteria. It is a resilient and robust structure developed for the protection from external stresses, the pursuit of nutrients, and to maintain environmental conditions necessary for the population to thrive (cf. Figure 1-1) [82]. When bacteria form biofilms, they are more resistant to antibiotics, predatory bacteria, the immune response of a host, changes in temperature, fluid flow, and nutrient deficiency. There are metabolic and genetic differences between bacteria in a biofilm and the same species of bacteria in their nearby planktonic state [82, 54].

Plaque is one of the easiest biofilms to conceptualize. Plaque is gingival and subgingival biofilm formed on teeth. The reason for brushing in a circular motion with bristles in addition to the use of dilute caustic soda or other chemicals (toothpaste) is that antibacterial washes alone can not penetrate the biofilm. Subgingival biofilms attach in many places that the biofilm functions like a composite material in resisting shear (brushing and flossing) from multiple directions. The biofilms attach on the roughened surfaces of teeth and branch to cover wide areas. These bacteria are mostly harmless and potentially beneficial while "swimming" in the mouth but become problematic when they "customize their living space". Everything from the chemicals used to makeup the biofilm to metabolic byproducts begin to become problematic when they are released in high concentration near the teeth. There are also opportunistic
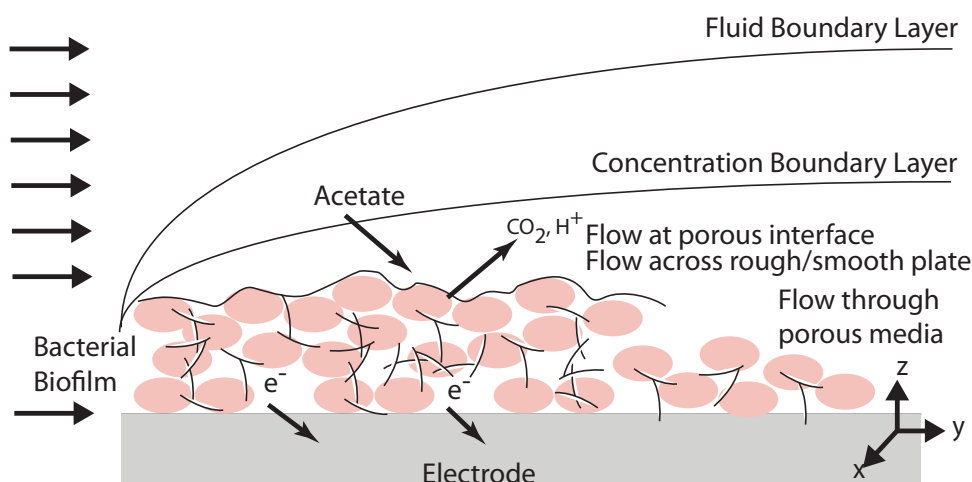
Figure 1-1: An illustration of the transport mechanisms through an electroactive biofilm. The structure is formed from bacteria and extracellular proteins secreted by the bacteria. The biofilm may entrap structures of the solid support material, like carbon nanotubes, surface roughness, etc. A biofilm regulates the environmental conditions the bacteria are exposed to such as: water content and flux, nutrient flux/storage, secreted regulatory chemicals, like those responsible for quorum sensing and antibiotic resistance. From a hydrodynamic perspective, the biofilm is an anisotropic poroelastic media. The porosity in the transverse direction increases or decreases depending on whether the support is the growth substrate or the substrate is in the fluid. The porosity in the lateral direction is typically greater and not as depth dependent. From a chemical perspective, the biofilm is an electrochemical catalyst and capacitor. Combined, the flow over the biofilm establishes a hydrodynamic and concentration boundary layer above and gradients of pressure and concentration within.

bacteria that target tissues and cells like *Porphyromonas gingivalis* that will attack young dendritic cells nearby.

Biofilms can incorporate multiple species of bacteria in symbiotic, mutually cooperative, or exploitative relationships. For example, layers of aerobic bacteria will form closer to the oxygen rich environments above layers of anaerobic bacteria and the metabolic byproducts will be shuttled between them. Biofilms made from multiple species of bacteria produce more power than biofilms formed from single species in microbial fuel cells (cf. Sec. 1.2.1), sometimes by an order of magnitude (Zhang et al. [93]). Certain species are better at anchoring to a substrate than others providing a nucleation point of the biofilm.

A biofilm is made from bacterial cells and extracellular polymer substances (EPS) including: exopolysaccharides like cellulose, proteins and nucleic acids. Biofilms exist in dry porous media like soil and in bodies of stagnant or moving water[16]. In adverse fluid flow conditions, biofilms form viscoelastic streamers, where the biofilm is only anchored at one point and extends into the flow [75, 86]. The viscoelastic properties of biofilms can sustain a streamer over a centimeter in length. Filamentous biofilms stretch over centimeter distances to move electrons from anoxic sediment to oxygen rich surface water [62]. Biofilms are more like vasculated tissue than gelatinous masses [80]. This vasculature varies in depth and direction and is explored in this thesis [88]. A combination of signaling, quorum sensing, cell-cell signaling, metabolite sensing or cell death, helps to determine biofilm structure [79].

Biofilms form and maintain existence by many different methods and more methods are being discovered. Bacteria in biofilms are very different from their planktonic cousins. They turn on and off up to 10% of their genome, a larger percentage than could be explained by swimming or sticking [54]. They have complicated communication methods that are involved in turning on and off EPS production [82, 37]. There are signaling pathways that can cause biofilms to stop formation all together. Scientist and engineers are trying to exploit the mechanical and biological properties of biofilms for our benefit.

1.2 The Importance of Biofilms

1.2.1 Energy - Water Nexus

The present study on biofilms targets Microbial Fuel Cells as a model platform. Microbial fuel cells have been considered a key component for bridging the energy/water nexus because of the relationship between biofilms and water treatment. Water treatment consumes over 3% of the total energy consumed in the United States [2]. This level of energy demand is impossible to meet for the developing world and is a global problem since inadequate treatment leads to disease and death [56]. Biological treatment is used to remove most organic and some inorganic chemicals in wastewater whether it is treated in a compost, septic tank, municipal or industrial wastewater treatment plant [24, 87]. Biological treatment reactors are designed to produce thin, but not abundant biofilms to expose bacteria to as much of the wastewater as possible for the amount of time required to reduce the pollutant load to safe limits [24, 39]. Byproducts of these processes include useful methane gas and biomass that can be turned into fertilizer. Other byproducts are sulfur dioxide, silicon dioxide, ammonia that limit the use of the synthesized methane as fuel. Microbial fuel cells are a useful way around this limitation since they produce power directly from the wastewater.

A microbial fuel cell (MFC) is a device where bacteria consume sugar and other hydrocarbons and 'excrete' CO_2, protons and electrons. A typical biofilm formed during operation of an MFC is shown in Figure 1-2 The electrons travel to corrosion resistant metals (the anode) while the protons diffuse away from the bacteria to be combined, at another electrode (the cathode), with the electrons that have passed through a circuit to generate useful work. MFCs are not a new technology, but interest in them has shown a resurgence in light of the current energy crises and UN development goals [69, 5, 56]. Research in the area has achieved power densities as high as $5\,\mathrm{W}\cdot\mathrm{m}^{-2}$ and continues to increase. Although power densities may not achieve independence from fossil fuels, they could power a lightbulb so that people can use the bathroom in places without electricity while simultaneously reducing

16
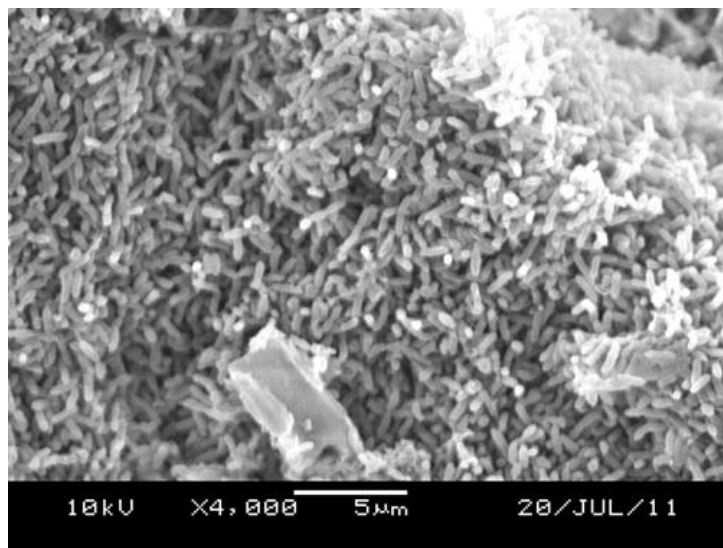
Figure 1-2: A scanning electron micrograph of *Geobacter sulfurreducens* strain PCA (the rod-shapes) biofilm on a carbon paper electrode (covered except the 4 μm wide object at the bottom of the figure). Cells were fed sodium acetate and grown on pH 7.2 phosphate buffer.

infectious pollutants in places without plumbing [4].

Microbial fuel cells face many challenges including the design of a hydrodynamic architecture that maximizes waste consumption, minimizes oxygen contamination, and maximizes the proton transfer [47]. This is not that different from the challenges faced by wastewater treatment plants [44]. The use of standard wastewater treatment architecture, for example anaerobic sludge blankets and up-flow suspended reactors, has been tried with limited success [26, 41]. This is partially due to the fact that those systems were not optimized to transfer current and the internal resistance is high. Designs that are being tested at present include connected porous matrices that will need models like the one developed in this thesis and others[64, 22, 67].

The anode of microbial fuel cells must be designed to maximize power production and waste consumption. In other words, the Coulombic efficiency and power density must be optimized. A survey of research data shows many different versions of carbon and other materials have been used as the anode and cathode materials although none have demonstrated consistent optimal performance (cf. Figure 1-3). Carbon is the cheapest, noncorrosive, conductive material that can be used in a microbial fuel cell
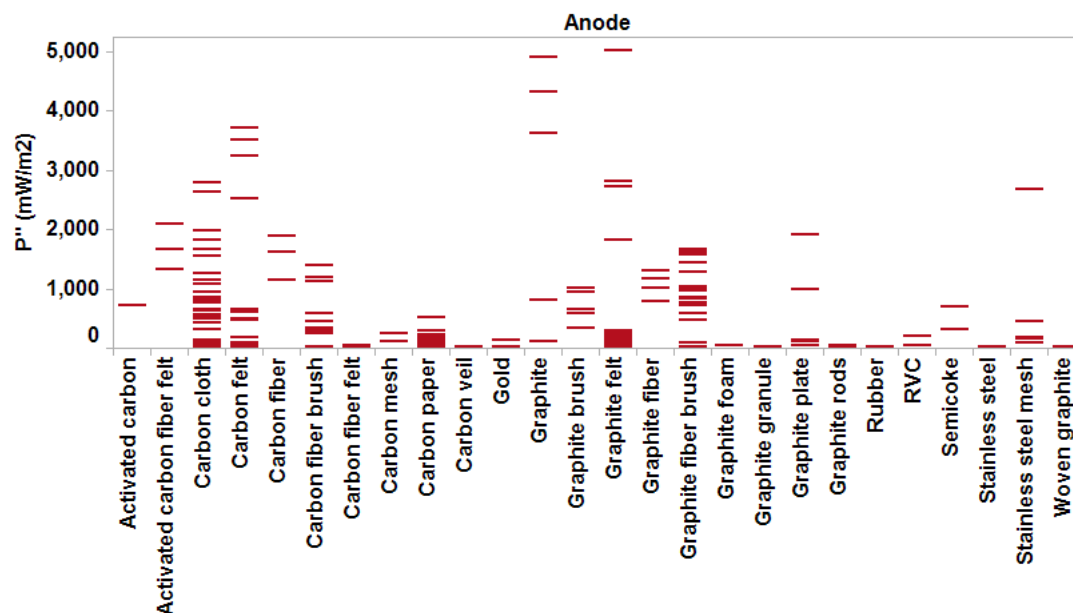
Figure 1-3: Survey of power density (by area) versus anode material type from literature published between 2002-2010 where each line is a maximum power density from a given study. While the standard purpose of graphing data is to show a trend, the purpose here is to show there is no clear correlation between material and power density. The high frequency of studies using carbon-based anodes is due to its low cost and many factors (manufacturing, pretreatment, size, etc) that can be varied. This two parameter analysis does not take in to account the different shapes of reactors and different species of bacteria and there is little data or mechanistic models to allow for a parameter that could.

Table 1.1: The metals utilized in this study. The conductivities, except silicon and pyrolytic graphite, are obtained from [25]. The conductivity for silicon and pyrolytic graphite are from the manufacturer. The commodity prices are from the latest version of [1].

Material	Group	Atomic #	Resistivity[Ωm10^{-8}]	USD/kg
Chromium	6	24	12.6	13
Copper	11	29	1.712	110
Silver	11	47	1.617	870
Gold	11	79	2.255	50k
Zinc	12	30	6.01	0.15
Titanium	13	81	23.8	27
Pyrolytic Graphite	14	6	100	3.00
Silicon	14	14	N/A	2.86
Stainless Steel 304	N/A	N/A	7200	3

(cf. Table: 1.1). Carbon's performance is limited by a relatively high resistivity. The performance of carbon can be enhanced by different production methods that increase its surface area.

1.2.2 Microbial Induced Corrosion

Corrosion in aquatic environments is problematic for pipelines, power plants, and other machinery that use water as a working fluid. Due to the ubiquity of microbes it has been difficult to distinguish corrosion from microbes and corrosion from the aquatic environment. Microbial induced corrosion can be caused by the creation of acidic and/or alkaline environments by the biofilm through the production of NH_4 and H_2S. Ennings et al. determined that microbial induced corrosion (MIC) by sulfate-reducing bacteria (SRB) is due to electrons being pulled from iron in pipes not hydrogen sulfide corrosion [20]. They tested pure cultures of *Desulfopila corrodens*, *Desulfovibrio ferrophilus*, and *Desulfopila inferna* cultured in control media with 10 mM acetate and on mild steel EN in artificial seawater media with 1mM acetate. Iron had to take part in the reaction since the strains did not produce H_2S without iron. *D. corrodens* and *D. ferrophilus* produced corrosion "crust" on the mild steel coupons. *D. inferna*, a hydrogen scavenger did not produce any corrosive crust. Scanning electron

micrographs showed crust formation, bacteria colonization (not necessarily a biofilm), "gas vents" and places of no crust formation. Energy dispersive X-ray spectroscopy showed that the location of no crust formation was identical to locations of no sulfur. After 150 days, *D corrodens*, *D ferrophilus*, and *D inferna* had reduced the mild steel to 27.8%, 68.1% and 98.8% of their original volume respectively. The crust had a conductivity of $\sim 50\,\mathrm{S}\cdot\mathrm{m}^{-1}$. The reaction rates were faster than what could have happened during hydrogen sulfide corrosion. The vents appeared to be used for pH balance, but this was not confirmed experimentally.

1.2.3 Medical Biofilms

1.7 million infections and 99,000 associated deaths occur due to healthcare associated infections in American hospitals [38]. Biofilms are present in pneumonia, urinary tract surgical site and blood stream infections that may lead to thrombosis or sepsis. Biofilms form in several places: on epithelial or endothelial lining, teeth and implanted medical device (IMD) surfaces; in lung, intestinal or vaginal mucus layers, and intracellularly [11]. Due to the symbiotic, mutually cooperative, or exploitative nature of biofilm communities, many of the infectious bacteria are not culturable and not treatable.

The human immune response to surgery and IMDs can cause greater harm to the body. The first step in healing injured tissue is the accumulation of platelets and neutrophils. Macrophages are then recruited by chemical signaling. IMDs, in particular, are coated with proteins and glycoproteins such as: fibronectin, vitronectin, fibrinogen, albumin, and immunoglobulins. Bacteria would not be able to attach to many bioengineered surfaces without this protein coating. Furthermore when exposed to the host's immune response (e.g., antibodies) biofilms will grow thicker. Certain bacteria have even been shown to intentionally recruit host cells in order to start growing a biofilm.

Specific instances of a biofilm saving bacteria are examples of *Pseudomonas aeruginosa* being saved by its exopolysaccharide alginate matrix from IFN-γ mediated leukocyte killing[43]. While leukocytes can penetrate *Staphylococcus aureus* biofilms

that are 7-days old when grown in laminar shear, they cannot penetrate 2-day old biofilms grown in static fluid[42]. Biofilms are not simply benign harborers of hungry bacteria. *Porphyromonas gingivalis* produces a specific type of lipopolysaccahrides that stunts the growth of dendritic cells. Other *P. aeruginosa* biofilms form "mushroom explosions" and engulf neutrophils that had settled on their surface.

Detection of biofilms is mostly via the analysis of biological fluids, a step of which includes culturing the unculturable. There has been some success in *in vivo* studies including measurement of GFP fluorescing bacteria and immune-quantum dot labeling but these are limiting. "The 'holy grail' of biofilm infections is an early-warning diagnostic method that would allow for non-invasive detection of the early stages of tissue or biomedical implant infection and an expedient response"[11]. As shown in the next section, most methods of studying biofilms do not allow for *in situ* monitoring. Any *in vivo* methods of determining whether an infection existed at all would require greater understanding of the biofilms response to any such sensor, a topic addressed in the modeling section.

1.3 Methods for studying biofilms

Biofilms require the development of specific tools for study because they are not simply a collection of planktonic cells. Tubular and annular reactors have been used in most biofilm studies. The tubular reactor pumps nutrient water through a tube, similar to most applications, allowing for measurement of changes in heat transfer and studies of the biofilm under fixed hydraulic retention times. Annular reactors are the same 2 cylinder devices used for studying shear and are highly sensitive. Biofilm volume is measured by submerging a bare coupon of the material under test and a coupon with biofilm in water. Biofilm height has been measured using microscopy, moving from the focal plane of the biofilm to the focal plane of a clear acrylic slip, but this technique is error prone [15]. Biofilm height is also measured using conductivity probe, by inserting the probe in situ down to the height of the biofilm, the accuracy relative to a Vernier micrometer is 5%[15]. Biofilm mass is measured by

weighing a dried biofilm sample, removing the biofilm and weighing again. Indirect methods for measuring the biofilm include staining the exopolysaccarhides, measuring the chemical oxygen demand and the total organic carbon according to Standard Methods (cf. [70]). Counting and measurement of ATP since ATP is only present in live cells has also been used [15]. Oxygen and pH probes can be used in active biofilms to determine metabolic rates.

Microfluidic devices have been used to study biofilm formation on scales more relevant to bacteria. Kim et al. used a microfluidic device to determine how the biofilms of *Pseudomonas aeruginosa* (PA14) (surface) area changed as a function of Reynolds number finding both linear and exponential scalings [34]. Porous and tortuous environments found in nature have been mimicked with microfluidic devices for easier modeling and experimentation[75, 86]. Lam et al. designed a multilayer microfluidic device to control the concentration of oxygen in a upper gas layer that diffused to a lower media transport/culture layer. They were then able to grow *E. coli* (a facultive anaerobe), *F. nucleatum* (a strict anaerobe), and *A. viscosus* (a strict aerobe) simultaneously [40]. Kim et al. created a gradient generator for Isatin, an indolin promoter, and 7-HI an indolin inhibitor, from $0 - 200 \, \mu M$ and $0 - 500 \, \mu M$ respectively in the same device growing *E. coli* [33]. The biofilm was suppressed and enhanced with regards to the pure promoter or inhibitor concentration gradients. When using competing gradients (both increasing), Isatin was able to offset the detrimental effect of 7-HI but the thickness decreased from the control showing that 7-HI was dominant. Using cross-mixed (decreasing Isatin, increasing 7-HI) the biofilm thickness increased from control showing that Isatin was dominant at greater or equal concentrations to 7-HI. Tests like these are can help target biofilms' response to a host immune response.

The electrical signal from a microbial device can be used to monitor changes in chemical composition of the feed water. With this in mind, a microbial fuel cell can provide a direct signal of biofilm health and metabolism. For example, as the biofilm produces more current it actually produces more protons than it can buffer that can easily be seen as a drop in current production [49, 6].

1.4 Present models of biofilm dynamics

A working group reported on the current state of biofilm modeling in Eberl et al. [19] with a few exceptions. This section highlights some points that are included in the model developed in this thesis (cf. Sec. 2.4). The utility of a biofilm is based on its metabolism and the efficiency of mass transport to the biofilm. To determine both metabolism and substrate transport, the structure of a biofilm must be ascertained. A biofilm's structure is a balance between transport, growth, detachment, and death. Electroactive biofilms are constrained by an electron acceptor potential, creating a unique addition to their metabolism and hence their structure.

1.4.1 Growth

Models of biofilm growth begin with the standard Monod model, [53]

$$\frac{\partial X_f}{\partial t} = Y \frac{q_m c}{K_m + c} X_f, \tag{1.1}$$

where for biofilm density X_f there is a yield Y when grown on a substrate c. The maximum rate the substrate is used is q_m (the utilization rate), which can be seen in the limit of large c. The half maximum concentration is K_m, which can be seen if $c = K_m$. The limiting relationship between oxygen (electron acceptor) and sugar (electron donor)can be modeled by multiplying Monod type expressions together. While this model does account for substrate utilization and limitations it does not include the death of bacteria. The biofilm will reach a steady-state, but would never die. To account for this, Rittman & McCarty included a decay rate,b, [74]

$$\frac{\partial X_f}{\partial t} = Y \frac{q_m c}{K_m + c} X_f - b X_f. \tag{1.2}$$

While not the first to do so, they also included Fickian diffusive transport of the substrate,

$$\frac{\partial c}{\partial t} = D \nabla^2 c - \frac{q_m c}{K_m + c} X_f \tag{1.3}$$

where D is the diffusivity of the substrate throughout a given medium. This model can be extended to multiple species of bacteria by including more equations for X_{f_i} with different utilization rates and different yields as simulated by Wanner & Gujer and simulated and experimentally verified by Rittman & Manem [90, 73].

A slightly different approach is to model the biofilm as a series of discrete particles, a cellular automata approach. While growth of the bacteria still follows the Monod kinetics model including death, this happens in discrete control volumes. At each iteration in time the biofilm density in a control volume is checked against a threshold density. If it exceeds the density, then it is randomly redistributed to the surrounding control volumes. The biofilm evolution can be coupled with either discrete or continuous models of substrate and liquid distribution. This approach was used by Picioreanu et al. to create the first 2D and 3D models of biofilms [67]. Their first simulation agreed well with experimental results for biomass growth in gel beads. The 3D simulation did much better than 2D because the 2D model did not account for growth into control volumes from out-of plane locations. Experimental and numerical substrate utilization (oxygen consumption) were in agreement using the 3D simulation, although there was no measurement of error. Cellular automata models have an advantage over continuum models in that bacteria are indeed discrete particles. But, as discussed earlier, biofilms are more than aggregates of bacteria.

1.4.2 Detachment

At this point, there is no mention of the biofilm's local environment. To account for environmental stress, Rittman introduced further loss rates R_T in addition to death,

$$
R_T = \begin{cases} -X_f L_f \left[b + s_1 \left(\frac{\gamma}{1+s_2(L_f - L_c)} \right)^{s_3} \right] & \text{if } L_f > L_c \\ -X_f L_f \left[b + s_2 \sigma^{s_3} \right] & \text{if } L_f \leq L_c \end{cases} \tag{1.4}
$$

that includes a loss due to a rate of shear γ of a biofilm of thickness L_f, where L_c is a critical biofilm thickness and s_i are a set of fitting parameters [72]. Many organisms respond to environmental stress with a change in metabolism, for example

hibernation of plants and animals in response to temperature stress. Shear rate should affect an active biofilm's metabolic activity, that is, its substrate utilization, substrate utilization rate, and the metabolic pathways taken. While a direct relation between shear rate and metabolic activity (substrate utilization) has not been found, a relation between substrate utilization, biofilm thickness and aerial biofilm density was found within a 95% confidence interval [85, 61]. The following equation is an exponentially damped equation

$$L_f = A - (B + Cq_m)e^{-kq_m}. \tag{1.5}$$

where q is the substrate utilization rate and A-C are experimental constants. Or, as It has been found that biofilm density changes in response to shear stress bulk metabolic activity may remain constant while local metabolic activity may change [61, 58]. The last two equations are empirical relations that are not well suited for modeling so that when Chang & Rittman did include shear stress, they only included it as a constant [14]. Picioreanu et al. introduced a more mechanistic approach to shear by using the von Mises criteria for plane shear stress,

$$\sigma_{xx}^2 + \sigma_{yy}^2 - \sigma_{xx}\sigma_{yy} + 3\sigma_{xy}^2 > \sigma_t^2 \tag{1.6}$$

where $\boldsymbol{\sigma}$ is the stress tensor, and σ_t is the tensile strength of the biofilm while the remainder of the model follows the discrete model they introduced previously [65]. This was based on observation by Ohashi & Harada that biofilms deform like elastic materials [60, 59]. This model viewed the biofilm as a homogenous isotropic material not accounting for biofilm porosity and its effects as will be discussed later. The model did predict the "avalanche" effect where biofilm downstream from a recently removed "shielding" section of biofilm are removed when they encounter a higher shear flow than they are used to. The model also predicted that faster growing biofilms are sheared off faster. It also correctly predicts "mushroom" behavior of biofilms under nutrient starved conditions where biofilms will create large mushroom shaped cavities before rupturing. This was duplicated using a continuum approach by Duddu et al.

showing that the results of this component was not an artifact of the numerical model chosen [18].

1.4.3 Structure

A biofilm is a heterogenous poroelastic medium. Porosity in biofilms is a little understood and rarely modeled phenomena [19]. While the concept of biofilm density is a recognition that biofilms are not solid, the consequences of this are not used in biofilm models. Wanner et al. created a model from conservation,

$$\frac{\partial \phi}{\partial t} + \frac{\partial j}{\partial z} = R \tag{1.7}$$

where $\phi = (AX_{F,i}, AS_{F,i}, A\varepsilon_{F,i})$ for the films (F) biomass, substrate, and porosity respectively for multiple species i [91]. In this model, advection is synonymous with growth displacement, the pore space and fluid volume shrink and expand respectively with growing and decreasing biomass. Diffusion is interpreted as a lumped parameter including "advection and migration" [91]. Flow through porous media is typically a more complicated process where dispersion, a phenomena due to advection, will depend on the velocity of the fluid and the medium will induce flow through pressure gradients even if there is no bulk flow [92].

Wanner & Guger updated their earlier model based on the observation by Stoodley et al. that there was flow through the biofilm. In this experiment, they defined mixed-culture biofilms of *P. aeruginosa*, *P. fluorescens* and *K. pneumoniae* in a polycarbonate conduit with recycled flow. Liquid velocity was measured using PIV and a confocal microscope. Fluid flow was found to occur throughout the biofilm to biofilm-to-void ratios as low as 0.05. The velocity through the biofilm was even found to go against the bulk flow. These experiments showed that flow through a biofilm is nonzero at a free stream velocity of $0.06\,\mathrm{ms}^{-1}$. van Wey et al. presented the most compelling evidence for including porosity in biofilm models. Confocal laser-scanning micrographs of six distinct aerobic bacterial biofilms were taken and deconstructed using MATLAB. A Monte Carlo random walk was used to estimate the diffusion

coefficient, where the walker would stop at each obstacle. Taking the mean squared difference of the tracer path, the tortuosity, τ of the biofilm was found. While values for the tortuosity in the direction parallel to the substrate line up well with Maxwell's equation

$$\tau = \frac{2\varepsilon}{3 - \varepsilon} \tag{1.8}$$

values perpendicular to the substrate do not. Values from previous literature all followed the parallel case. Porosity data was fit with an exponential. These three values were averaged over depth, so while not height specific, the results captured the anisotropy. These values were then included in a reaction-diffusion model with a Monod reaction. The experimental data showed parabolic curves for nutrient transport through biofilms grown on soluble substrates indicating that the biofilm is not as compact as previously thought. When grown on an insoluble substrate, the nutrient transport rapidly dropped by the middle of the biofilm. The results agreed well when compared to literature using stoichiometry for oxygen uptake.

1.4.4 Bioelectrochemistry

To use a microbial fuel cell (MFC) as a tool to study biofilms or for optimization of MFCs, electrochemical models need to be included. Kinetics modeling often follows that of standard fuel cells with some modification. Hamelers et al., compared the use of a Butler-Volmer-Monod (Eq. 1.9) to a Nernst-Monod model (Eq. 1.10) for kinetics of MFCs. The Butler-Volmer-Monod model uses Butler-Volmer kinetics in the Monod expression for maximum substrate utilization to determine current

$$\frac{I}{I_{max}} = \left(\frac{1 - e^{-V_t^{-1}\eta}}{K_1 \cdot e^{-(1-\alpha)V_t^{-1}\cdot\eta} + K_2 e^{-\alpha V_t^{-1}\eta} + 1} \right) \cdot \left(\frac{c}{\frac{K_M}{K_1 \cdot e^{-(1-\alpha)V_t^{-1}\cdot\eta} + K_2 e^{-\alpha V_t^{-1}\eta} + 1} + c} \right), \tag{1.9}$$

where I is the current, I_{max} the maximum current, η is the overpotential, the difference between the actual and the standard voltage, $V_t^{-1} \approx 26\,\text{mV}$ is the thermal voltage, $\alpha \approx 0.5$ is the charge transfer coefficient and K_1, K_2 are reaction rates dependent on the concentration. The Monod constant K_M can be related through fitting to

the Monod constant K_m in the standard Monod model. The Nernst-Monod model is similar,

$$\frac{I}{I_{max}} = \left(\frac{1}{1 + e^{-V_t^{-1}\eta}}\right)\left(\frac{c}{K_m + c}\right).$$ (1.10)

The model uses two steps: bio-chemical substrate oxidation and electron transfer. Specifically, there is a three-step reaction model between acetate and the final redox step of an unspecified redox component (electron mediator). The models were fit by minimizing the residual sum of squares between the analytical expression and a set of concentration dependent MFC experiments. The Butler-Volmer-Monod model did add to the accuracy of the potential dependence of the Monod constant (appears circular). Due to the dependence on fitting, the model is both highly specific and accurate. Due to the analytical nature of the model, it is possible to apply it to any polarization curve data. Current density as a function of concentration was not as easily fit to the data, but this was not explained [23].

Marcus et al. similarly used a Monod model for reaction kinetics (derived from Rittman [74]) incorporating the size of the biofilm [49, 50]. To include this, the model assumed a homogenous biofilm conductivity over both active and inactive bacteria but a volume fraction of active bacteria mass for the purpose of kinetics. The active biomass was calculated based on Wanner & Gujer including growth, respiration and decay [90]. Conservation of charge also had to include the fractional usage of electrons for bacterial growth. Substrate diffusivity into the biofilm was included with a diffusivity included from Ebrel, et al[19]. The model was extended to include the transport of protons through the biofilm and the impact of low pH on biofilm activity.

Strycharz-Glaven et al. considered the electrical kinetics of the biofilm, particularly the conductivity of the transmembrane proteins that appear to be responsible for electron transfer both embedded within the biofilm and as isolated "nano-wires"[83]. In their work, the electrode and the cell were considered at fixed potentials.The proteins were considered to be made of uniformly spaced of distance δ chains of redox species of total concentration $C_T = C_{red} + C_{ox}$ with equal reaction rate k_0 for both

reduction and oxidation. A fractional electron transfer rate was modeled

$$X_{1,2} = \exp\left(\frac{nF}{RT}(E_{1,2} - E^{0'})\right) \tag{1.11}$$

where $E_{1,2}$ was the potential of the electrode and membrane respectively. The model predicated current for the proteins embedded in the biofilm of

$$i = \frac{nFAk_0 C_T^z \delta}{w}\left(\frac{1}{1 + X_1} - \frac{1}{1 + X_2}\right) \tag{1.12}$$

where $i_L = \frac{nFAk_0 C_T^z \delta}{w}$ was considered as the experimental fitting parameter, thus limiting the impact of including many of the parameters.Yet this model did fit the data well relative to the competing model developed for an isolated nanowire excited by a potential V/W,

$$i = 2nFAC_{red}C_{ox}k_0 \sinh\left(\frac{nF}{2RT}\frac{V}{W}\delta\right). \tag{1.13}$$

The first 2D simulation of an MFC was by Picioreanu et al. using a Butler-Volmer model for the reaction kinetics of an electron mediator. Reaction of the substrates to form biomass and reduce a mediator then provided the link between the Monod model for biofilm growth and the Butler-Volmer model. These models included acetate, protons and hydroxide, and a carbonate buffer. The pH of the solution was used since the redox reaction rate of the mediator is dependent on pH similar to Marcus et al. [63, 64, 66]. The latest model did include a flow field but did not include its affect on the biofilm geometry or the biofilm's geometry's affect on the flow field.

1.5   Thesis summary

Biofilms are communities of bacteria that respond dynamically to varying environmental stresses. They are present everywhere including in places where we want them, like wastewater treatment, and in places we do not, like in our pipes and blood streams. A fuller understanding of biofilms will help us more efficiently interact with

them if we are trying to do things like implement them in microbial fuel cells or remove them from the human body. The tools that to study are beginning to scale down from "large" reactors to length scale where we can see how they adjust at their time frame. The models, and our ability to solve those 3D coupled models, are beginning to explain some of the phenomena surrounding the biofilms response to chemical stresses. We must now begin to look at how they respond to mechanical stresses with our new tools.

A new tool to study biofilms is developed in the present study. The device is designed with materials compatible for biofilm growth and compatible with light and confocal microscopy for direct measurement of the growing biofilm. It is also designed to incorporate indirect methods of biofilm health like substrate utilization (chemical oxygen demand measurement), and pH change. As a microbial fuel cell and another indirect method of monitoring biofilm health, the device is designed to measure total current and potential of individual electrodes. To interpret these results, a model is developed that incorporates biofilm growth from a continuous perspective, the biofilm response to shear stress, and as an addition to existing models, biofilm growth and response to shear as a poroelastic medium. The device is then tested with one type of electrode and one flow rate. Preliminary data is presented to guide further experiments on biofilm substrate compatibility, a biofilms response to shear, and the optimization of a microbial fuel cell.

Chapter 2

Methods for studying biofilms

2.1 Microfluidics

Microfluidics have been used for precision control of liquids and gases in small devices. Microfluidic devices, like the one presented here, have at least one critical dimension that is between $10 - 100\,\mu$m [51]. These devices have a wide range of geometries and configurations ranging from high-aspect ratios to multiple channels to embedded electrodes. Modeling the flow through these devices can also range from simple Navier-Stokes flow with rectangular boundary conditions to much more complicated models [21].

Most microfluidic devices are governed by laminar flow due to the critical dimension. Under laminar flow control it has been possible to deposit or etch material on to or from the surface of channels with a thickness equal to that of the laminar flow boundary layer. For example, electrically continuous silver wire has been deposited on glass, gold has been etched from gold, and silicon has been etched from silicon [78, 32]. These latter processes were accomplished at the diffusion boundary layer between two parallel reactants flowing under laminar conditions. Using the same physics, laminar-flow fuel cells (LF-FCs) have been designed to separate the desired reactions on opposite sides of the separating diffusion boundary layer. These devices establish laminar-flow between two streams flowing horizontally parallel in shaped 'Y'-channels, 'T'-channels, and vertically parallel in 'L'-channels [36, 35, 30]. These

fuel cells have a high volumetric power density and lower internal resistance than fuel cells where the reactants are separated with a physical barrier.

The advantages to studying microbes and biofilms in a microfluidic device were explained in Section 1.3. There are also benefits to the direct electrical signal from microbial fuel cells as an indicator of metabolism (cf. Section 1.2.1). A laminar flow microbial fuel cell (LF-MFC) combines all the properties above into a unique tool for studying biofilms.

2.2   Design, Manufacturing, and Materials

2.2.1   Design

This LF-MFC is an x-shaped channel. This design separates the outlet into 3 streams: a consumed anolyte, a consumed catholyte, and a mixed stream. Channel geometries were tested numerically to maximize electrode surface area and minimize cross-over without including reaction kinetics (COMSOL Multiphysics, Sweden).The 3D numerical simulation includes free fluid flow and flow through a porous media to simulate a non-active biofilm. An active biofilm would consume the concentration the chances for cross-over would decrease. The porous media was $10\,\mu$m tall, had a 50% porosity, a $0.7\,\mathrm{m}^2$ permeability and covered the entire anode. These conditions are an approximation of a biofilm. The resulting channel has a 1.1 mm width over the 20 mm of fully developed channel length without cross-over. The electrodes are $0.3{\times}20\,\mathrm{mm} = 6.0 \times 10^{-6}\,\mathrm{m}^2$ spaced 0.5 mm apart. The channel height is $55\,\mu$m. The inlets and outlets are angled and the corners rounded to reduce secondary flow. Rounded corners are also simplify manufacturing and numerical meshing. The velocity is slightly lower over the porous matrix in simulation, Figure 2-1. The diffusive mixing region is fully encompassed by the 3rd outlet channel in the simulation Figure 2-2.

Carbon deposited onto glass and onto patterned gold; carbon mixed with poly(dimethyl siloxane) (PDMS); standard PDMS covered gold electrodes on glass; carbon rods embedded in PDMS; carbon in PDMS and acrylic based devices were either developed
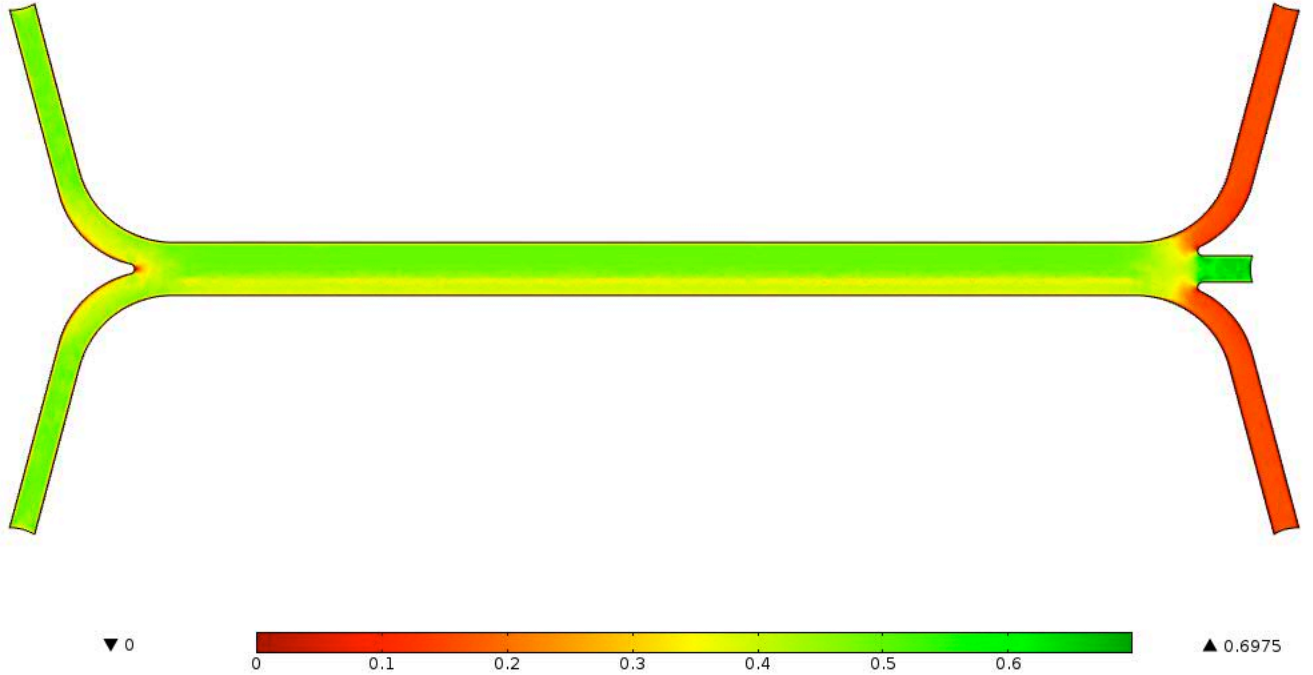
Figure 2-1: The fluid velocity $[\text{m}\cdot\text{s}^{-1}]$ distribution at the centerplane of the channel. The velocity is slightly lower over the porous matrix (the bottom half of central channel) used to simulate the biofilm than over the smooth cathode region. Channel geometries were tested numerically to maximize electrode surface area and minimize cross-over.The numerical simulation included free fluid flow and flow through a porous media to simulate a non-active biofilm. The chances for acetate cross-over would be reduced when an active biofilm was consuming it. The porous media was $10\,\mu\text{m}$ tall, had a 50% porosity, a $0.7\,\text{m}^2$ permeability and covered the entire anode. These conditions are an average approximation of a biofilm. The channel has a 1.1 mm width over the 20 mm of fully developed channel length without cross-over. The electrodes are $0.3 \times 20\,\text{mm} = 6.0 \times 10^{-6}\,\text{m}^2$ spaced 0.5 mm apart. The channel height is $55\,\mu\text{m}$. The inlets and outlets were angled and the corners rounded to reduce secondary flow. Rounded corners were also useful for manufacturing and numerical meshing.
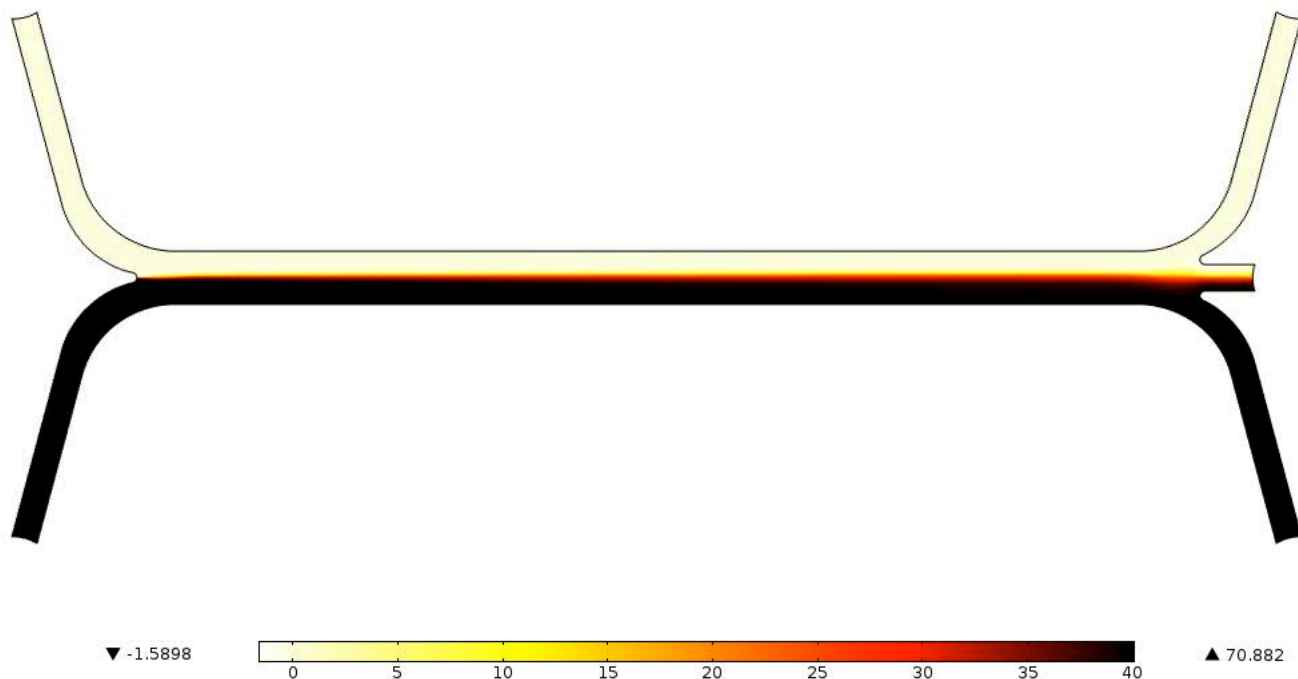
Figure 2-2: The concentration of acetate (in mM) flowing through and diffusing across the channel layer. The mixing region is fully contained in the mixed outlet channel and the concentration of acetate is negligible over the area in which the cathode is placed. Channel geometries were tested numerically to maximize electrode surface area and minimize cross-over.The numerical simulation included free fluid flow and flow through a porous media to simulate a non-active biofilm. An active biofilm would consume the concentration the chances for cross-over would be less. The porous media was assumed to cover the anode at $10\,\mu$m tall, 50% porosity, and $0.7\,\mathrm{m}^2$ permeability. These conditions are an average approximation of a biofilm. The channel has a 1.1 mm width over the 20 mm of fully developed channel length without cross-over. The electrodes are $0.3 \times 20\,\mathrm{mm} = 6.0 \times 10^{-6}\,\mathrm{m}^2$ spaced 0.5 mm apart. The channel height is $55\,\mu$m. The inlets and outlets were angled and the corners rounded to reduce secondary flow. Rounded corners were also useful for manufacturing and numerical meshing. The mixing region is fully encompassed by the middle channel.
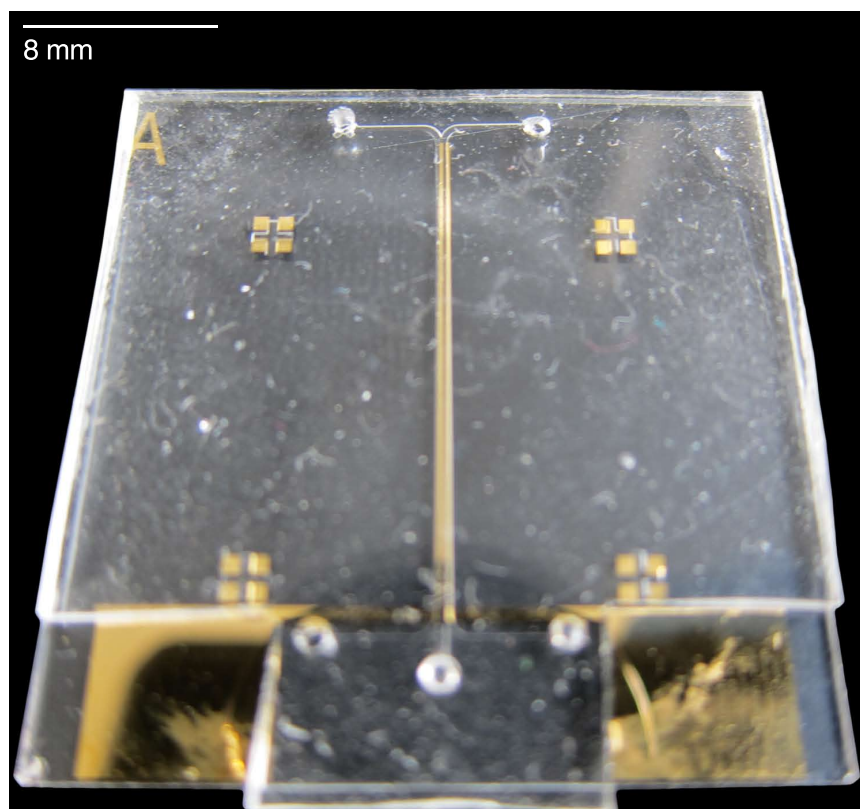
Figure 2-3: Microfluidic devices are commonly made from PDMS since it can be rapidly prototyped using photolithography. Similarly, gold electrodes are commonly used with microfluidic devices since they can also be rapidly patterned using photolithography. The device shown here has two parallel electrodes leading out to foot pads that can be connected to an external measurement device. This device was abandoned because bacteria do not adhere as well to gold as they do to carbon.

herein or duplicated herein in order to include different metals into the laminar-flow microbial fuel cell. Each method will be briefly explored to help explain the final design.

Microfluidic devices are commonly made from PDMS since it can be rapidly prototyped using photolithography [76]. Similarly, gold electrodes are commonly used with microfluidic devices since they can also be rapidly patterned using photolithography. An LF-MFC device made using this process, shown in Figure 2-3 has 2 parallel electrodes leading out to foot pads that can be connected to an external measurement device and a 1 cm thick PDMS cap. This would not be effective since bacteria do not adhere as well to gold as they do to carbon [71]. In addition to gold, indium tin oxide,

aluminum, chromium, an silicon can all be micro-patterned using photolithography which may be a viable option if bacteria can be acclimated to those substrates.

Standard lithographic techniques can be used to produce carbon electrodes. Yet this method is time consuming. Sputter coated graphite can be produced using two graphite targets in an 80% Argon 20% Nitrogen environment with a DC and RF power source at 250 W for 52 minutes in an AJA international Orion 5 to produce a 200 nm thick layer. The amorphous carbon produced is not conductive. A novel way around this is to deposit a conductive layer first under the graphite layer as done in Figure 2-4. Gold was initially deposited onto patterned photoresist using electron-beam deposition and then developed. Carbon is then deposited onto the entire wafer. This is then patterned again. The non-patterned graphite is removed using oxygen plasma. The resulting carbon deposited will not be the same as graphite or most common forms of carbon and the presence of the underlying conductive layer will definitely impact any the electrochemical/catalytic activity of the assembly. Yet, the resulting assembly is conductive and usable in a PDMS-based device. There are other means of making gold a biocompatible electrode including the use of self-assembled monolayers of thiols and carbon nanotubes but these avenues are not practical for scale-up.

Carbon Black powder was blended with poly(dimethyl siloxane), its linking agent and toluene, a thinning agent, as a material for micro-patterned electrodes [57], Figure 2-5. In Figure 2-5 (A) a 10 w.t.% carbon black in PDMS resulted in a conductivity of $2.97 \, \text{nS} \cdot \text{cm}^{-1}$. In Figure 2-5(B), an increase in concentration to 20 w.t.% carbon black resulted in a reasonable conductivity $2.3 \, \text{mS} \cdot \text{cm}^{-1}$ but the material was too stiff to be patterned into anything useful as seen by its inability to mold to the petri dish. These results agree well with those in Niu et al. who preceded to use silver nanoparticles to enhance the conductivity. This method could not be done for biocompatible applications. Future use of this type of micro-patterning could benefit from using gold or iron nano-particles, the latter to increase biocompatibility. The design in Figure 2-6 is limited in electrode material. This can be overcome by placing a physical barrier between two pockets, Figure 2-7. Two pockets 4 x 20 mm, large
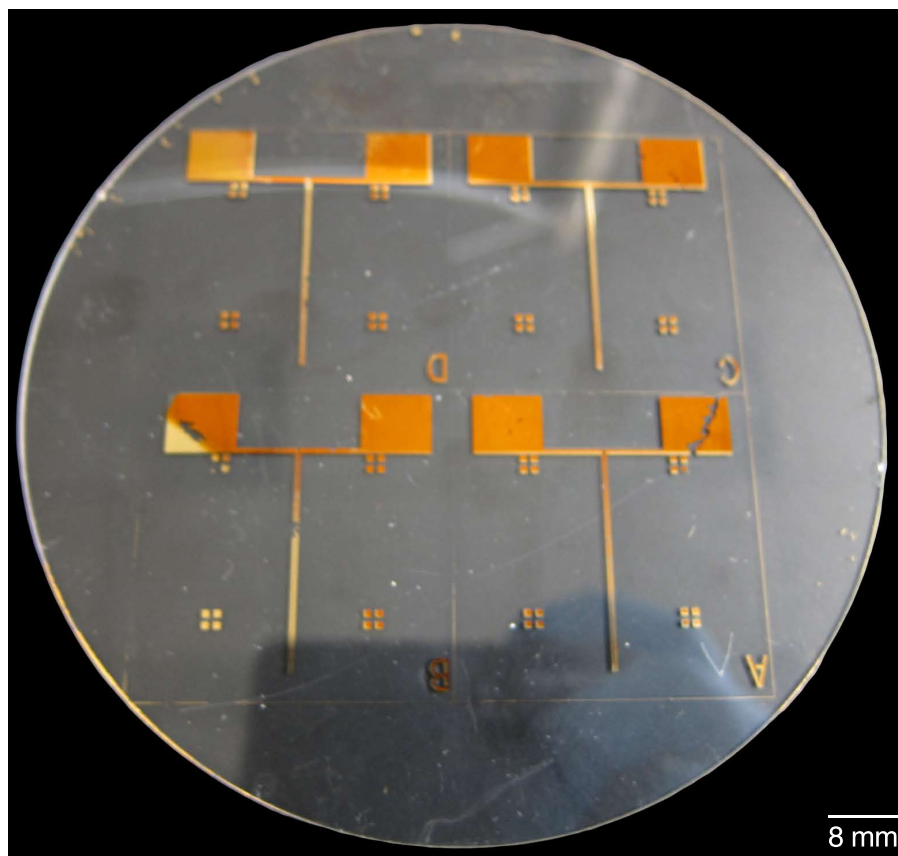
Figure 2-4: A novel though costly method of producing micropatterned, conductive, carbon is presented in this figure. Gold was initially deposited onto patterned photoresist using electron-beam deposition and then developed. Carbon is then deposited onto the entire wafer. This is then patterned again. The non-patterned graphite is removed using oxygen plasma. The resulting carbon deposited will not be the same as graphite or most common forms of carbon and the presence of the underlying conductive layer will definitely impact any the electrochemical/catalytic activity of the assembly. Yet, the resulting assembly is conductive and usable in a PDMS-based device. There are other means of making gold a biocompatible electrode including the use of self-assembled monolayers of thiols and carbon nanotubes but these avenues are not practical for scale-up.

Figure 2-5: Carbon Black powder was blended with poly(dimethyl siloxane), its linking agent and toluene as a thinning agent as a potential material for micro-patterned electrodes [57]. In (A) a 10 w.t.% carbon black in PDMS resulted in a conductivity of $3.0\,\mathrm{nS \cdot cm^{-1}}$. In (B), an increase in concentration to 20 w.t.% carbon black resulted in a reasonable $2.3\,\mathrm{mS \cdot cm^{-1}}$ but the material was too stiff to be patterned as seen by its inability to mold to the petri dish. These results agree well with those in Niu et al. who preceded to use silver nanoparticles to enhance the conductivity that is not applicable for biocompatible applications [57]. Future use of this type of micro-patterning could benefit from using gold or iron nano-particles, the latter to increase biocompatibility.

Figure 2-6: To address the problem of oxygen leakage that PDMS has, the same microfluidic device as Figure 2-3 was made from acrylic. The device reduced manufacturing time using a shadow mask for non-lithographic patterning of electrodes. The materials that could be used would still be those made through physical vapor deposition.
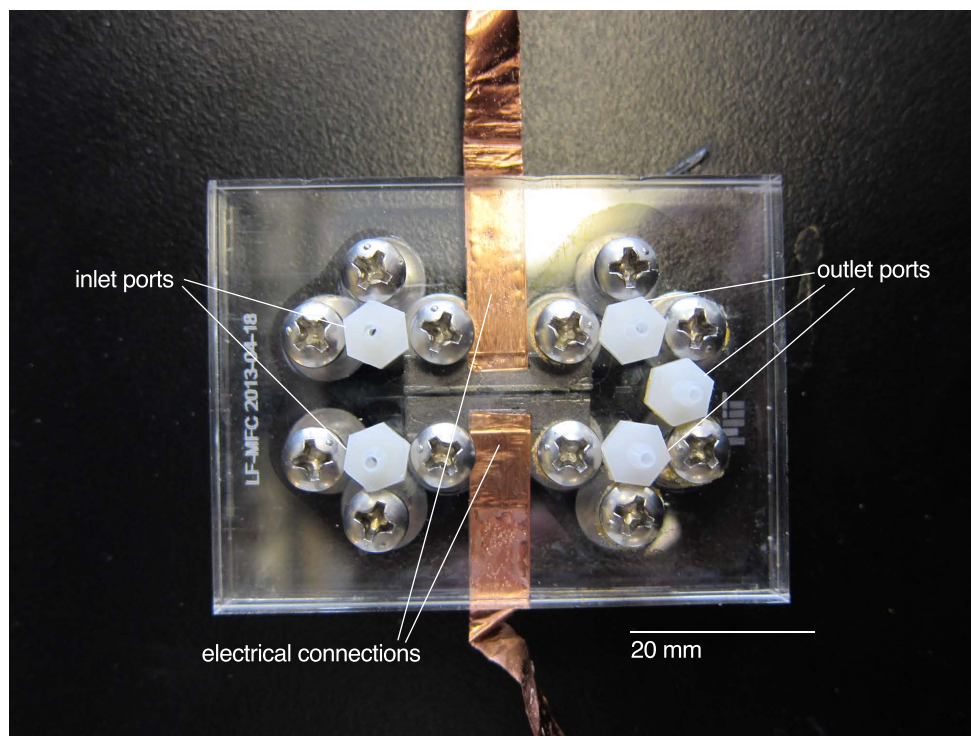
Figure 2-7: The final design of the Laminar-Flow Microbial Fuel Cell consists of two 4 x 20 mm pockets to hold electrodes at 0.4 mm apart. This is capped with a channel layer that is ported with autoclavable barb-tub connectors and copper electrode connectors. A seal is achieved with 12x 6-32 screws, tightened until Newton rings are visible.

enough to be handled and cut, spaced 0.4 mm apart were milled into the base layer. When capped with the channel layer, they have an electrode area that is only 0.3 mm where the total channel width is 1 mm wide. The maximum distance between the 6-32 thread screws was found experimentally to be 6.25 mm. At this distance, the destructive interference of Newton's rings predominated the constructive interference verifying that the gap between the two pieces of acrylic was as close as possible. The ports are 10-32 threaded PTFE barb-tube connectors that could be autoclaved. The additional screws are needed to seal the edges around the tube connectors.

2.2.2   Manufacturing

The LF-MFC is designed as a tool to study *in situ* electroactive biofilm formation. The LF-MFC is cut from cast acrylic, poly(methyl methacrylate) (PMMA). PMMA has a refractive index of $n_D^{25} = 1.49$[3]. PDMS has a refractive index of 1.403. While the refractive index of PDMS is closer to that of water, the working fluid, PMMA is closer to that of glass used in microscopes so there is a trade off either way. The water absorption of both PDMS and cast PMMA is between 0.2 - 0.8% so there is no difference. The gas diffusion rate of oxygen through acrylic is $3.3 - 33 \times 10^{-9}\,\mathrm{cm^2 \cdot s^{-1}}$ [27]. The gas diffusion rate of oxygen through PDMS is $3.4 - 16 \times 10^{-5}\,\mathrm{cm^2 \cdot s^{-1}}$[8]. The high oxygen diffusion rate in PDMS is typically used to help grow aerobic bacteria and human tissue. This 4 orders of magnitude difference between acrylic and PDMS can mean the difference between life and death for strict anaerobic bacteria [77, 40]. PDMS was used as the channel material for the other two LF-MFCs that exist which may explain their low current generation [45, 46]. [1]

The top and bottom half of the LF-MFC are cut from cast acrylic using a laser cutter (Epilog Laser , USA). This allows for rapid cutting of the screw holes but not the channels since the machine's precision is $\pm 2\,\mathrm{mm}$. The channel and pockets are cut on a Microlution 363-S (Microlution, Chicago, IL, USA). The mill has a reported accuracy of $\pm 2\,\mu\mathrm{m}$ but, as will be shown, can be pushed into the 100 nm range. The tool parameters and setups are optimized to yield a smooth surface finish and preserve flow geometry. Any machining of a microfluidic device with similar features should use similar parameters. This mill is equipped with a 56,000 rpm, air-turbine spindle with a 3.175 mm (1/8") dia chuck, flood coolant and air coolant. The pallet working area is $60 \times 58\,\mathrm{mm}(x \times y)$ and a custom fixture was made to hold each part in place to preserve alignment. The rotational velocity is limited to 48,000 rpm to minimize wear on the spindle bearings. The channels are cut using a 0.254 mm (0.01in) 4 flute end mill. This was chosen over smaller end mills and 2 flute end mills to minimize
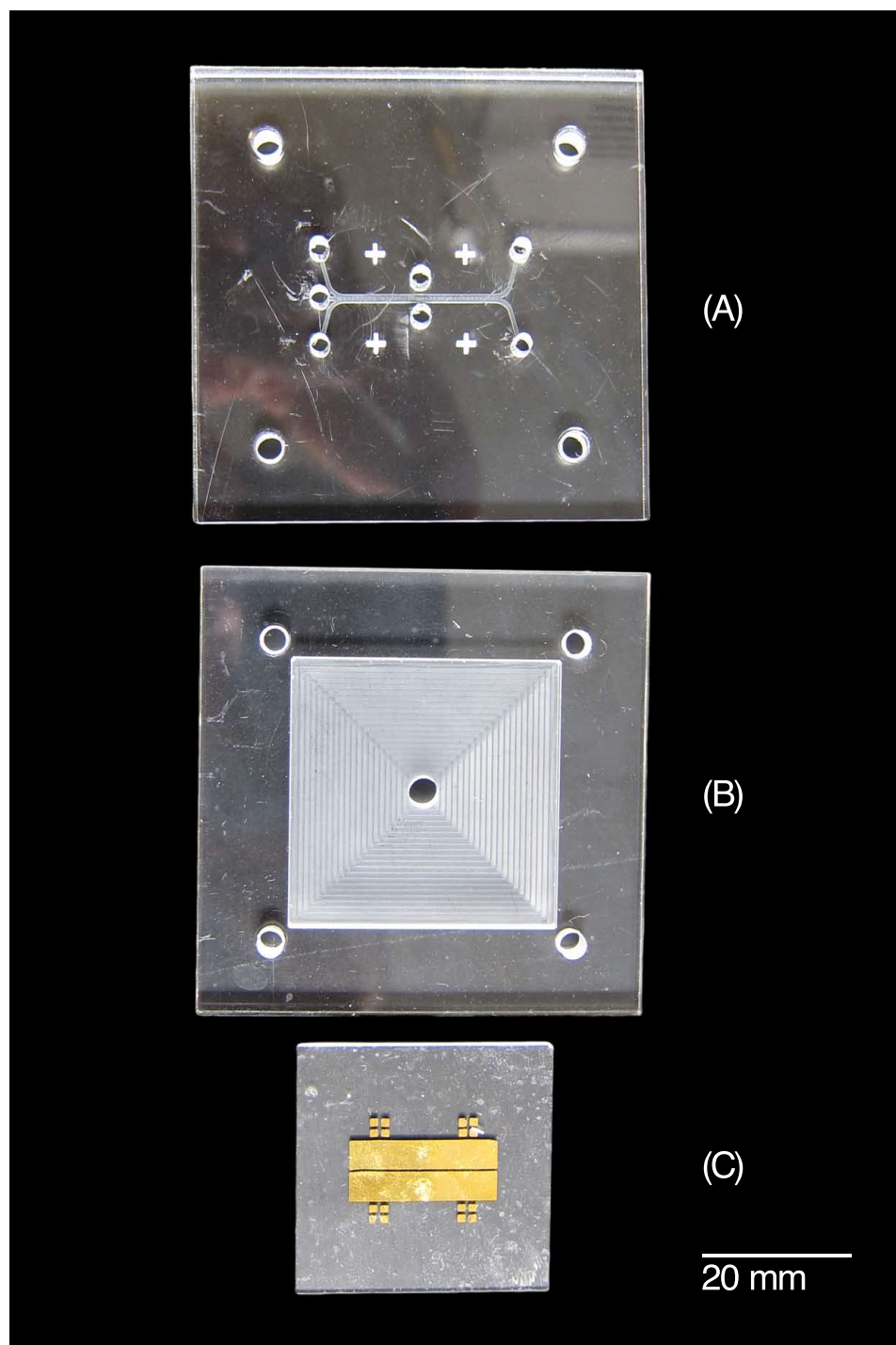
---

[1]To address the problem of oxygen leakage that PDMS has, the same microfluidic device as Figure 2-3 was made from acrylic. Manufacturing time was reduced by using a shadow mask for non-lithographic patterning of electrodes. The materials that could be used would still be those made through physical vapor deposition.

scalloping, the formation of ridges between cuts of a mill. The chip load, the size of chips cut by the each flute, is $1.9\,\mu$m/tooth which gave a feed rate of $365\,$mm/min. Optimization of the cutting parameters matched the formula found by Vogler et al.,

$$R_a \propto \frac{CL^2}{0.5D},\tag{2.1}$$

where R_a is the surface roughness, CL is the chip-load [μm/tooth], and D is the tool diameter [μm] [89]. A proportionality constant of 5 for acrylic was calculated by cutting with a 0.508, 0.381 and 0.254 mm (0.02, 0.015 and 0.01 in) diameter tools.

All mill paths and G-code are generated using MasterCam X5 (CNC Software, Inc, Tolland, CT, USA). The tool path for the channels is a "2D pocket Dynamic Area Mill." This produces an optimal path for cornering. A stepover of 5% diameter is used to minimize scalloping. Scalloping can be reduced by using a finish pass. Since the depth of cut for this part is $55\,\mu$m, any finish pass would produce nanometer sized chips that could not be properly cleared with flood coolant. Atomized coolant is recommended for clearing the small chips in micro-machining to improve surface finish, minimize tool wear and reduce part temperature. High temperature can cause the welding of chips to the part [31]. The mill used here is not equipped with atomized coolant but the measured surface finish is $\sim 100\,$nm and there is no indication of welded on chips. The representative area shown in Figure 2-8 is the tool entry point where the surface roughness is the largest. The path for the conductive tape electrical connector and electrode pocket is a parallel spiral without overlap since surface finish did not matter. A single spring pass of $10\,\mu$m is necessary for the large depth of the pockets and kept for consistency in the electrical connectors.

The electrode pockets are of variable depth depending on the electrode thickness as mentioned in Sec. 2.2.1. The pocket depth is $0.8\,$mm for glass coated electrodes. The depth is $0.1\,\mu$m for the pyrolytic graphite sheets. The pockets are cut to within $20\mu m$ using a 3.175 mm (1/8") dia 4 flute square end mill at 48,000 rpm and a feed rate of $244.44\,$mm/min for a 2% chip load followed by a $0.254\,$mm (0.1 in) dia 4 flute square end mill using the same parameters as above for deep pockets. After
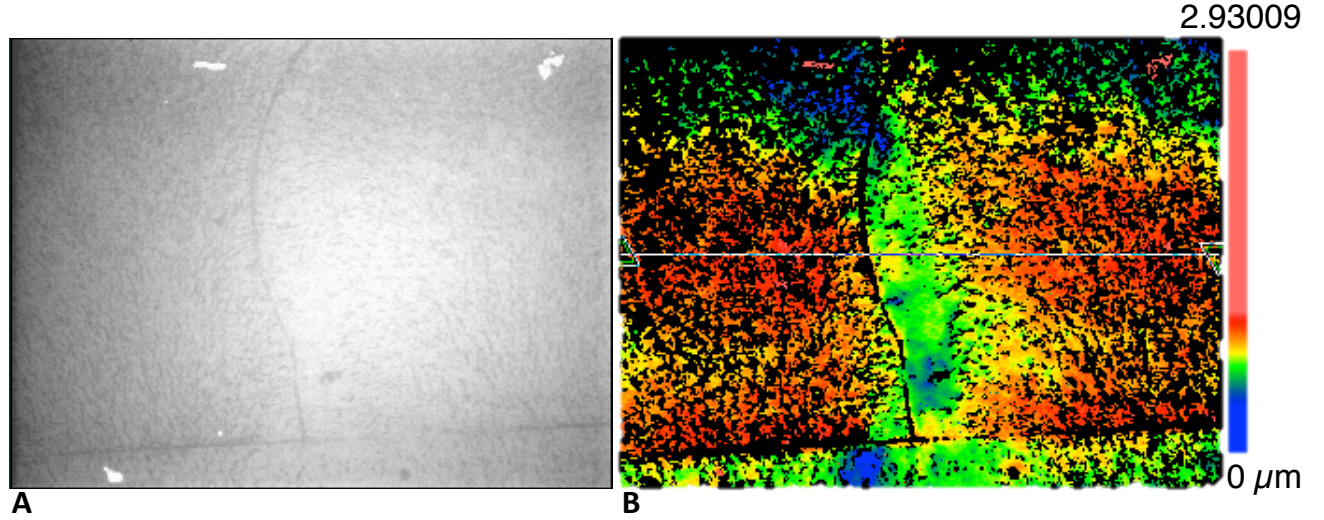
Figure 2-8: The representative area shown in Figure 2-8 is the tool entry point where the surface roughness is the largest. A gradient heat map of the height of the milled surface is shown in (B). The optical image of the same surface is shown in (A). The average surface roughness was calculated from this as ~ 100 nm.

machining the device, the parts are cleaned in a sonicator in Citranox ® to remove coolant oil and any chips leftover from the cutting processes. Ultrasonic cleaning is recommended to remove small ($< 2\,\mu$m) chips that could get stuck in the corners of the channels. Citranox ® is a organic acid cleaner and any remaining citric acid must be removed by thorough rinsing (sonication) with deionized water. A final polishing step is used to return the machined surface to its original clarity, Figure 2-9. The MIT logo appears foggy to the naked eye in image Figure 2-9(A) and remains even when the surface roughness is $\sim 100\,$nm. This can be eliminated with chemical vapor polishing using dimethylene chloride as shown in Figure 2-9(B) when then MIT logo almost disappears. The final channel height and the surface roughness are measured using an optical profilometer (NewView 600, Zygo, USA). The LF-MFC channels have an average height of $51.217\,\mu$m $\pm\,8.180\,\mu$m and an average surface roughness of $100.58\,$nm $\pm\,21.94\,$nm.

The device is assembled using 3.81 mm dia. 6-32 hex head screws with washers and hex-nuts to evenly distribute the compressive force until Newton's rings were visible around the channel and screw heads. The presence of the Newton rings ensured a

Figure 2-9: A final polishing step was used to return the machined surface to its original clarity. The MIT logo appears foggy to the naked eye in (A) and remains even when the 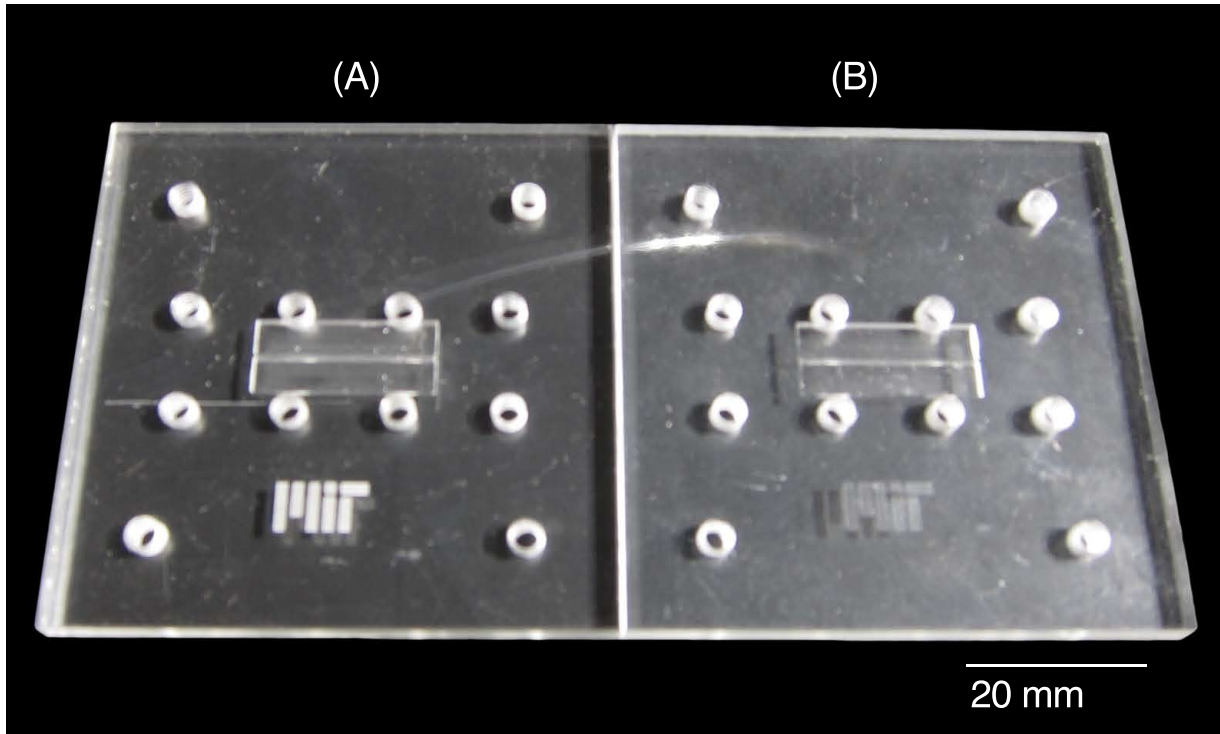surface roughness is ~ 100 nm. This can be eliminated with chemical vapor polishing using dimethylene chloride as shown in (B) when then MIT logo almost disappears.

seal. The channel inlets and outlets were 10-32 thread hose-barb tube connectors.

2.2.3   Materials

When bacteria colonize a surface they can cause a variety of problems and, in certain cases, some benefit. When bacteria colonize submerged or buried pipes with water or other substances through it, they can cause corrosion on the outside or inside[20]. In pipes, on ship's hulls and propellors biofilms can cause substantial drag losses. When bacteria colonize doorknobs, bench-tops and medical equipment they can increase the spread of disease. On the other hand, when bacteria colonize membranes in membrane biological reactors for wastewater treatment they decrease the footprint of water treatment plants.

The choice of substrate is critical to the cells growth and survival in an engineered environment[7]. When bacteria colonize insoluble electron acceptors, power can be harvested from them. The surface area of the substrate controls the upper limit of a monolayer of bacteria that can be in one device. The surface roughness, wettability, and electrostatic interactions determine whether or not the bacteria will bond to the surface [9]. The catalytic activity will determine the reversibility and viability of this interaction. Finally, the conductivity will determine how much current will be generated by the device. In order to quantify this interaction, multiple materials were tested in the same device.

All electrodes are cleaned in an ultrasonic bath in Citranox ®, acetone then iso-proponal for 5 minutes each. They are imaged using scanning electron microscopy (VEGA3 SEM, Tescan, CZE). Surface roughness is measured using optical profilometry. Atomic force microscopy in tapping mode (Nanoscope IV Dimension 3100 SPM, Veeco, USA) is used to measure the surface roughness for surfaces where the surface features were smoother than the resolution of the optical profilometer. Scanning electron microscope images of each surface are provided in Figures 2-10-2-11. Surface free energy is calculated using contact angle measurements on each substrate. Deionized water and ethylene glycol were used as the polar substances while 1-bromonapthalene is used as the polar substance. Variation in surface energy measurements is common.
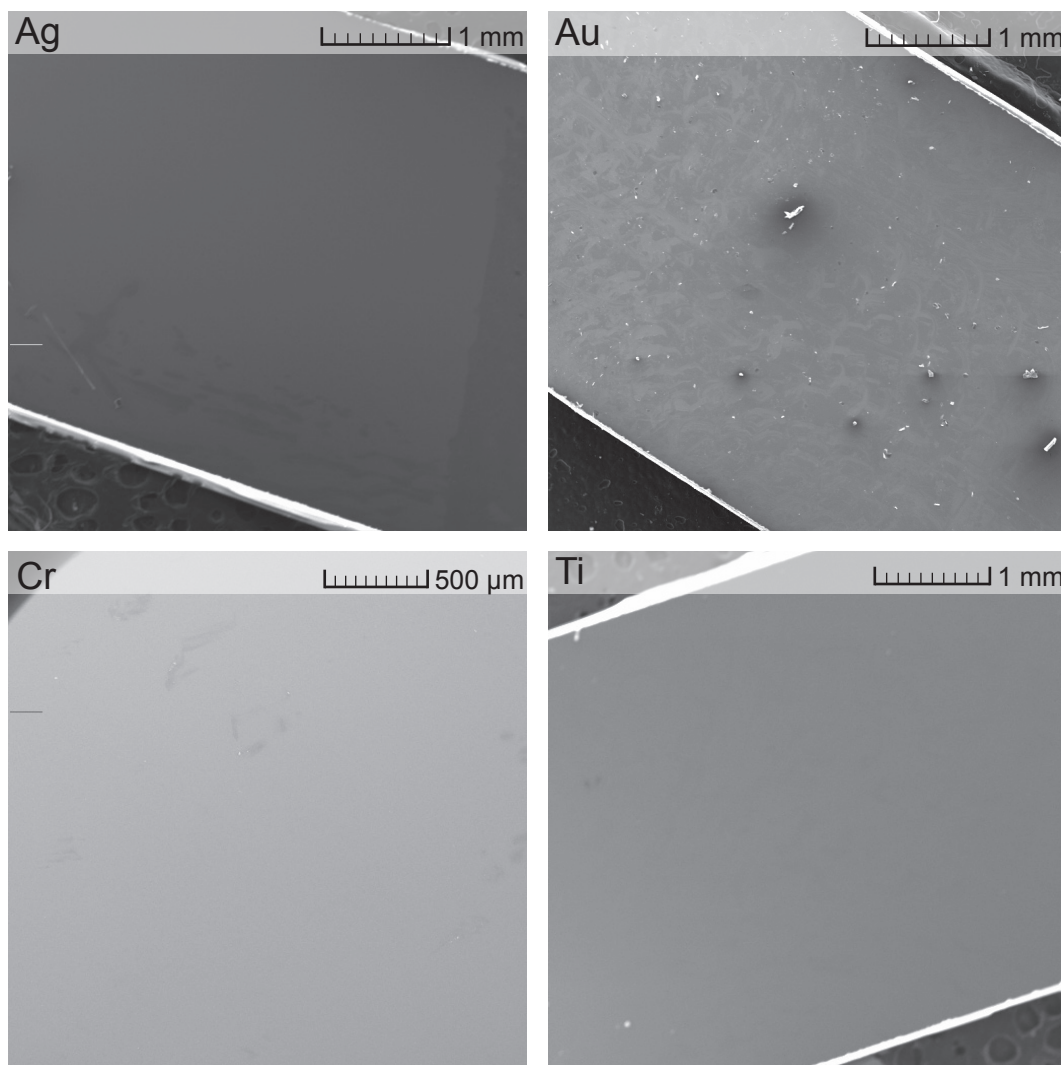
Figure 2-10: The SEM images of the electrodes after cleaning and before they were placed in the laminar-flow microbial fuel cell. The images show the relative surface roughness. The silver (Ag), titanium (Ti), chromium (Cr), and gold (Au) were deposited using electron-beam physical vapor deposition to thicknesses of 50 nm, 50 nm, 200 nm and 200 nm (with a 20 nm Ti base layer.)
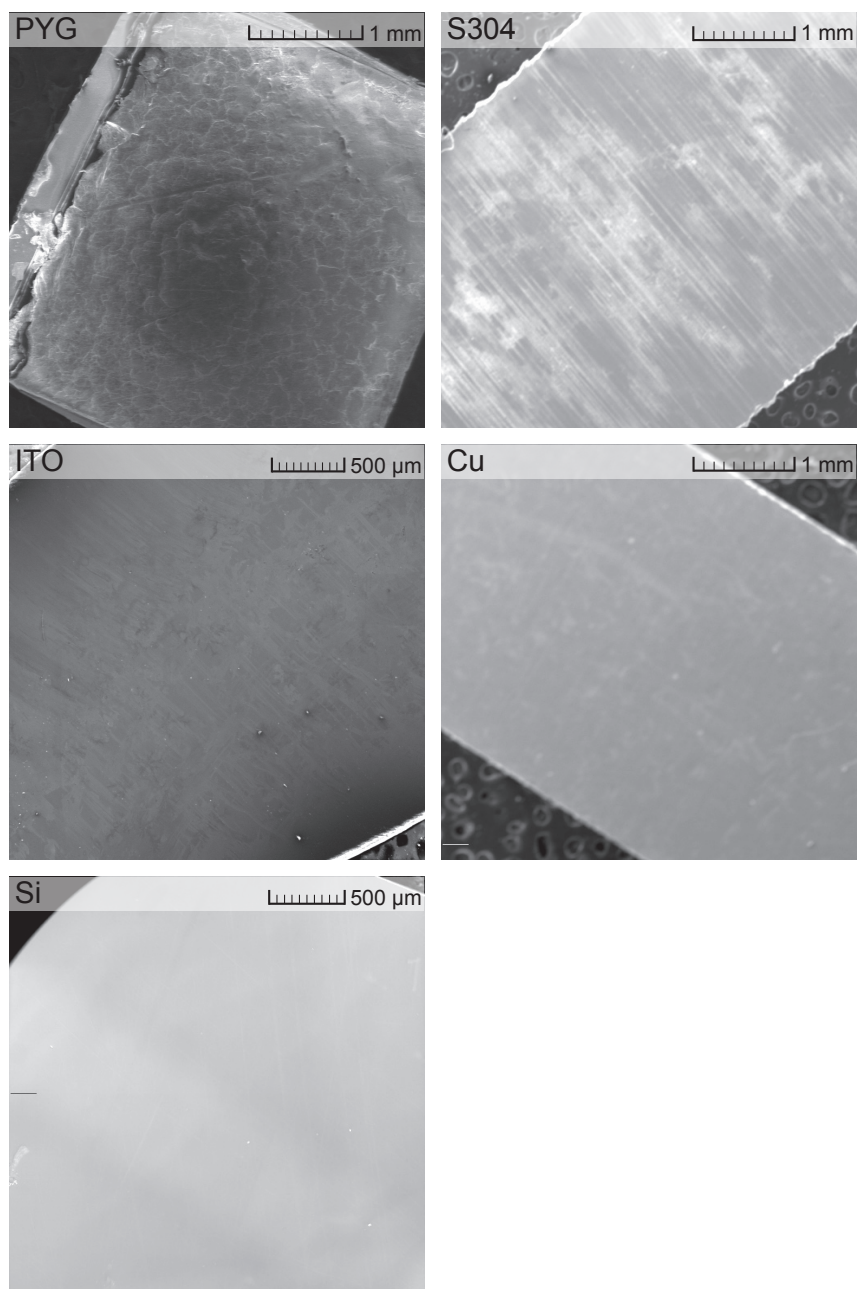
Figure 2-11: The SEM images of the electrodes after cleaning and before they were placed in the laminar-flow microbial fuel cell. The images show the relative cleanliness. The copper (Cu), indium tin oxide (ITO), stainless steel type 304 (S304), and pyrolytic graphite (PYG) were factory purchased. The copper and stainless steel were rolled sheets. The ITO was deposited onto clear PTFE in 120 nm layers. The pyrolytic graphite was nominally 100 μm thick with a 17 μ m adhesive layer, not measured as only the surface roughness was necessary.

Variations can be due to the anisotropy of the crystal surface of copper or zinc and the deposited nano-clusters of titanium, chromium, silver, or gold. This theory will not be corrected here and the results are used as is.

Interactions of the bacteria and the surface can be modeled using DLVO theory [16, 12, 28]. The surface energies of solids cannot be tabulated in the same way surface energies of liquids can be tabulated at specific temperatures due to interactions of the liquid with the crystal structure [17]. The liquid used to determine the surface energy, surface roughness, the orientation of lattice planes, and temperature can all impact the measurements. With the current models, surface energy calculations are useful for trends between materials, not rigid design parameters. Regardless of which model is used, the Gibbs Free energy of interaction, ΔG_{1234}^{TOT}, is the sum of all the Gibbs energy, ΔG_{1234}, in the system

$$\Delta G_{1234}^{TOT} = \sum \Delta G_{1234} \tag{2.2}$$

where 1 is the solid, 2, the liquid, 3, the particle, and 4, the vapor. In the present model,

$$\Delta G_{lsb}^{TOT} = \Delta G_{lsb}^{LW} + \Delta G_{lsb}^{AB} + \Delta G_{lsb}^{EL} \tag{2.3}$$

where l is the liquid medium, s is the solid substrate, b is the bacteria. The models are LW for Lipshitz- van der Waals interaction, AB for Lewis acid-base interaction and EL for electrostatic interaction. The Gibbs free energy between the liquid and the surface is

$$\Delta G_{ls} = \Delta G_{ls}^{LW} + \Delta G_{ls}^{AB} = 2 \left(\sqrt{\gamma_s^{LW}\gamma_l^{LW}} + \sqrt{\gamma_s^+\gamma_l^-} + \sqrt{\gamma_s^-\gamma_l^+} \right), \tag{2.4}$$

where γ is the surface free energy. This is related to the contact angle between the surface and liquid, θ through Young's equation

$$(1 + \cos\theta)\gamma_l = 2 \left(\sqrt{\gamma_s^{LW}\gamma_l^{LW}} + \sqrt{\gamma_s^+\gamma_l^-} + \sqrt{\gamma_s^-\gamma_l^+} \right). \tag{2.5}$$

Table 2.1: The properties of the liquids chosen to compute the surface free energy in Figure 2-12 as described in Sec. 2.2.3 from Hwang et al.[28].

Chemical	γ_l	γ_l^{LW}	γ_l^{AB}	γ_l^{+}	γ_l^{-}
α-Bromonapthalene	44.4	44.4	0	0	0
Water	72.8	21.8	51.0	25.5	25.5
Ethyelene Glycol	48	29	19	3.0	30.1
mJ $\cdot$ m^{-2}					

The LW component of the solid is found using a nonpolar substance, here 1-bromonapthalene (Sigma-Aldrich, MO, USA) is used for this measurement. Since the donor/acceptor energies for a nonpolar substance are $\gamma_l^{+} = \gamma_s^{-} \approx 0$,

$$(1 + \cos\theta)\gamma_l = 2\sqrt{\gamma_s^{LW}\gamma_l^{LW}}. \tag{2.6}$$

The electron donor/acceptor surface energies are found using two different liquids, water and ethyelene glycol so that,

$$\begin{pmatrix} \sqrt{\gamma_s^{+}} \\ \sqrt{\gamma_s^{-}} \end{pmatrix} = \begin{pmatrix} \sqrt{\gamma_{l1}^{-}} & \sqrt{\gamma_{l1}^{+}} \\ \sqrt{\gamma_{l2}^{-}} & \sqrt{\gamma_{l2}^{+}} \end{pmatrix}^{-1} \begin{pmatrix} 0.5\gamma_{l1}(1 + \cos\theta_1) - \sqrt{\gamma_s^{LW}\gamma_{l1}^{LW}} \\ 0.5\gamma_{l2}(1 + \cos\theta_2) - \sqrt{\gamma_s^{LW}\gamma_{l2}^{LW}} \end{pmatrix}$$

The parameters for the measurements are shown in Table 2.1. The results from these measurements reaffirm the common wisdom that stainless steel and carbon are more biocompatible for bacterial adhesion and copper is the least, Figure 2-12. The finding that silicon is also biocompatible may make micro-patterned devices possible. Further testing of these materials as discussed in Sec. 2.2.1 should be done to confirm that biocompatiblity is a function of surface energy.

2.3   Testing

The x-cell Laminar-Flow MFC is run from a 100 mL H-cell MFC using pressure driven flow, Figure 2-13. This allows bacteria from the macro anode to directly inoculate the micro-anode. Both cells are operated across a $1\,\mathrm{k\Omega}$ resistor. The anolyte
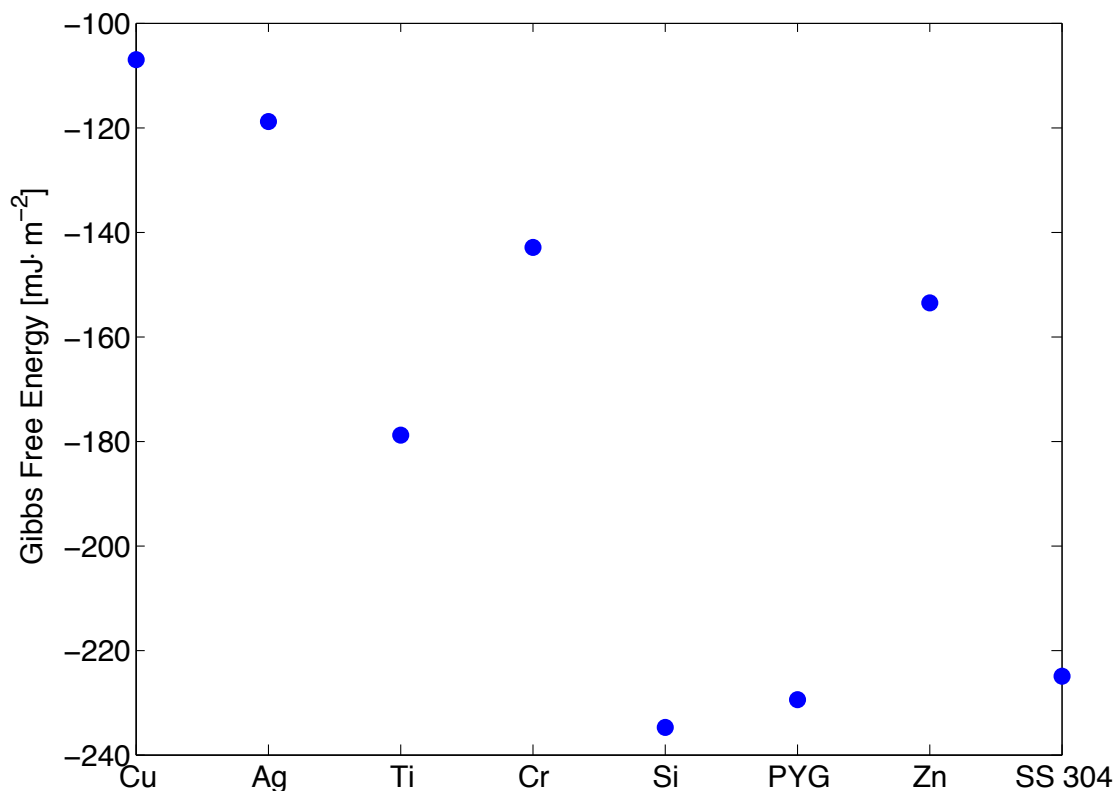
Figure 2-12: The Gibbs Free Energy of interaction of various materials. Contact angles were measured of deionized water, ethylene glycol and 1-bromonapthalene on all the substrates. 1-bromonapthalene is a nonpolar liquid where the other two liquids are polar. The latter allows for the separation of positive and negative surface free energy as described in Sec. 2.2.3. The more negative the surface energy, the more favorable the interaction. The results reaffirm the common wisdom that stainless steel and carbon are more biocompatible for bacterial adhesion and copper is the least. The finding that silicon is also biocompatible may make micro-patterned devices possible.

17.2 kPa (2 psi)

Macro - Microbial Fuel Cell

Computer

N_2

50 mM $K_3Fe(CN)_6$
Cathode

10 mM NaOAc + *G. Sulfurreducens*
Anode

LF-MFC

DAQ

Separated Waste

Not to scale
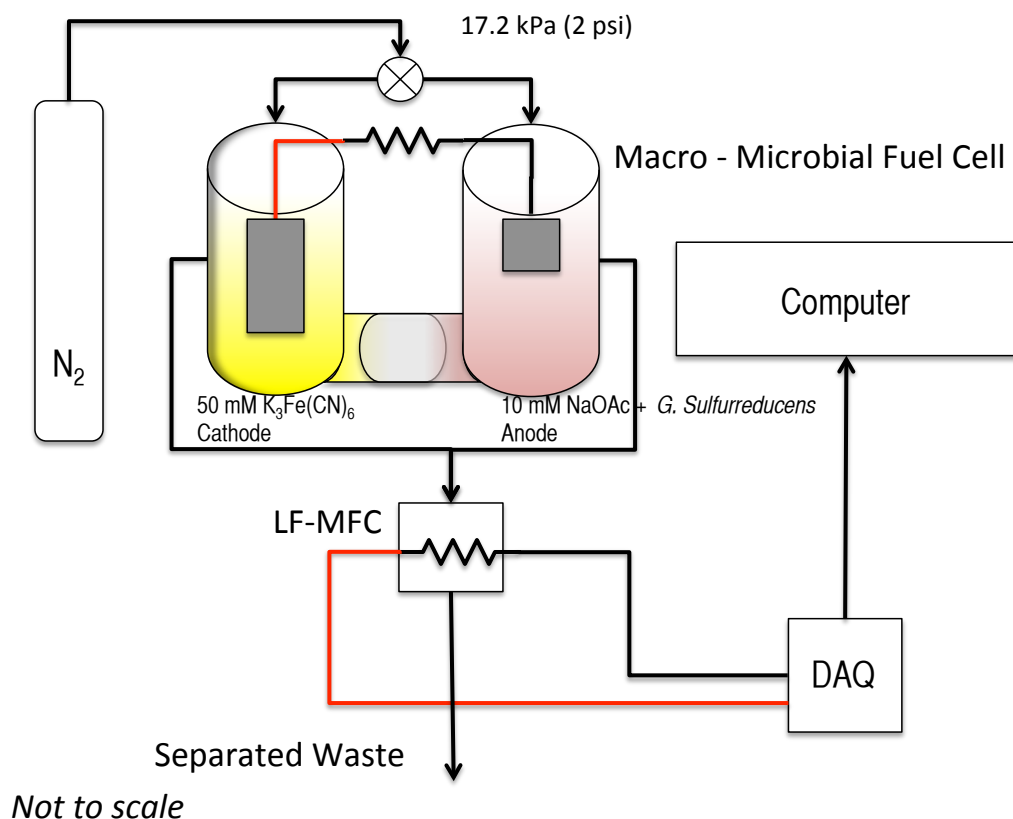
Figure 2-13: The x-cell Laminar-Flow MFC was run from a 100 mL H-cell MFC using pressure driven flow. For reference, the H-cell consist of two chambers separated by a proton exchange membrane (Nafion 117, Dupont). This method of flow allowed bacteria from the macro-anode to directly inoculate the micro-anode. Both cells were run across the same $1\,k\Omega$ resistor. The anolyte was 10 mM NaOAc and the catholyte was 40 mM $K_3Fe(CN)_6$. The flow rate of $60\,\mu L \cdot min^{-1}$ drained the H-cell in 27 hrs. The waste streams were separated into consumed anolyte, consumed catholyte and a mixed stream. This will allow future experiments to analyze metabolic byproducts. The electrical signal was measured using an analog-to-digital converter (USB6001, National Instruments,UK) and read by data acquisition system at 1 Hz (LabVIEW, National Instruments, UK).
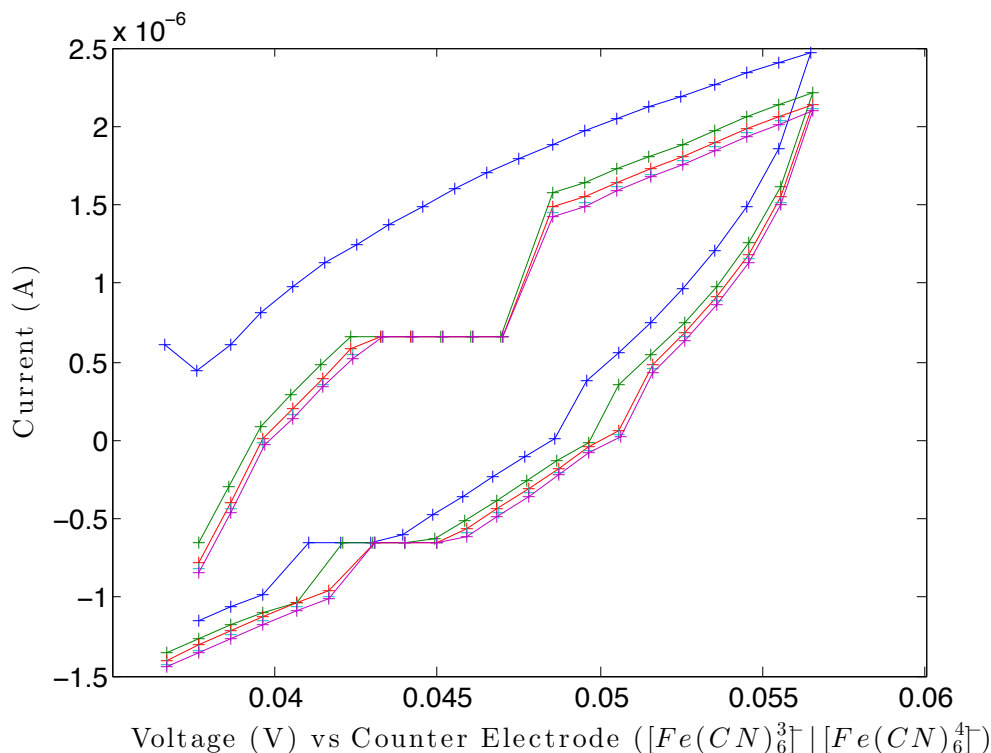
Figure 2-14: A baseline cyclic voltammogram without bacteria was determined for the LF-MFC. The scan rate was $75\,\mathrm{mV} \cdot \mathrm{s}^{-1}$ (Reference 600, Gamry Instruments, Philadelphia,PA USA). The CV does not show any appreciable redox peaks as expected. The electrodes were pyrolytic graphite. The fuel was run at $60\,\mu\mathrm{L} \cdot \mathrm{min}^{-1}$ from a syringe pump (PHD 2000, Harvard Bioscience, Holliston, MA, USA). The anolyte was 10 mM sodium acetate in a pH 7.2 phosphate buffer solution. The catholyte was 40 mM Potassium Ferricyanide in the same buffer solution.

is 10 mM sodium acetate and the catholyte is 40 mM potassium ferricyanide. The flow rate of $60\,\mu\mathrm{L} \cdot \mathrm{min}^{-1}$ drained the H-cell in 27 hrs. The waste streams were separated into consumed anolyte, consumed catholyte and a mixed stream. This will allow future experiments to analyze metabolic byproducts. The electrical signal is measured using an analog-to-digital converter (USB6001, National Instruments,UK) and read by data acquisition system at 1 Hz (LabVIEW, National Instruments, UK).

The bacteria were shown to be electrochemically active through cyclic voltammetry. A baseline without bacteria was determined for the LF-MFC, Figure 2-14. The electrodes were pyrolytic graphite. For the abiotic run, the fuel was run at $60\,\mu\mathrm{L}/\mathrm{min}$ from a syringe pump. The anolyte was 10 mM sodium acetate in a pH 7.2 phosphate

buffer solution. The catholyte was 40 mM Potassium Ferricyanide in the same buffer solution. The scan rate is 75 mV/s. The abiotic CV did not show any appreciable redox peaks so the cell was operating without any leaks of copper, oxygen, or cross-over.

2.4   Modeling biofilm dynamics

Current models of biofilm dynamics have divided biofilm activity into four processes: growth, detachment, structure and bioelectrochemistry (cf. Sec. 1.4). In this model, the fluid flow is assumed to control the growth, detachment and structure of the biofilm so such a division is not possible. The mass and fluid transport in a biofilm can be broken into transport through (1) the bulk system outside of the boundary layer, a distance $\delta = \max(\delta_m, \delta_l)$ away from the biofilm, (2) the mass and fluid boundary layer region of thickness δ_m, δ_l respectively, (3) the interface between the bulk and the biofilm, 4) the biofilm and 5) the biofilm electrode interface (cf. Figure 1-1). Furthermore, any biofilm process is a catalytic process subject to Michaeliis-Menten (Monod) kinetics, growth, death, and loss [68, 19]. In what follows the unsteady Stokes equation is used to establish the hydrodynamic boundary layer (1) and (2) from above. An advection-diffusion-reaction equation is then solved for solute to calculate the concentrations field of the mass transfer boundary layer. The porosity of the biofilm will determine the flow through the biofilm and is included as a source term. The relation between shear stress and biofilm loss has been experimentally determined, but existing models have come short of using structural properties of a biofilm to predict biofilm loss as a function of shear stress [74, 34]. Here, shear between the bulk flow and the biofilm defines the interface and also cell loss and growth by assuming the biofilm is a poroelastic medium. As mentioned in Sec. 1.3, a microbial fuel cell produces a direct electrical signal that is a function of: biofilm health, metabolism, and size. A description of a Butler-Volmer kinetic equation, interaction 5 in the above, is given here, not including mechanisms for electron conduction or capacitance, but not solved for.

2.4.1   Fluid Flow

The fluid subsystem can be modeled using the Navier-Stokes equation,

$$\left(\frac{\partial \mathbf{u}}{\partial t} + \mathbf{u} \cdot \nabla \mathbf{u}\right) = \nu \nabla^2 \mathbf{u} - \frac{1}{\rho}\nabla p - \frac{\nu}{k}\mathbf{u}, \tag{2.7}$$

for velocity vector $\mathbf{u}$, pressure p, ensemble (or solvent water) kinematic viscosity ν (or ν_0), and ensemble (or solvent water) density ρ (or ρ_0). The additional term on the right hand side is the Darcy pressure term used to find the velocity in the porous media with permeability k. Since the permeability is different in the $\hat{z}, \hat{y}$ directions, this term is more active in one dimension than the other. This equation is coupled with the continuity equation for an incompressible fluid,

$$\nabla \cdot \mathbf{u} = 0 \tag{2.8}$$

Equations 2.7 and 2.8 can be simplified by looking at the 2D problem, in dimensions $\langle y, z \rangle$ as shown in Figure 1-1. The equations can be further simplified through scaling analysis. Let the velocity scale in the direction of flow as $u_y = V\tilde{u}_y$ and $u_z = W\tilde{u}_z$ where V is the inlet velocity and the scaling of W will be determined later. D is the length of the biofilm so that the length scale along the direction of flow is $y = D\tilde{y}$ and $z = L_c\tilde{z}$ in the direction perpendicular to flow where L_c is a characteristic length. The characteristic length in the biofilm is the biofilm thickness, $L_c = L_f$. Biofilms tend to not form outside the viscous boundary layer of the fluid, so the characteristic length scale in the fluid is the boundary layer thickness $L_c = \delta_l$ along the biofilm (for biofilm streamers) or along the surface it is growing on. The characteristic time for the fluid is $\tau_l = \frac{D}{V}$. The latter scaling will be balanced with scaling of the biofilm growth and substrate transport later. Substituting these relations into Eq. 2.7 yields,

$$\left(\frac{V}{\tau_l}\frac{\partial \tilde{u}_y}{\partial \tilde{t}} + \frac{V^2}{D}\tilde{u}_y\frac{\partial \tilde{u}_y}{\partial \tilde{y}} + \frac{VW}{L_c}\tilde{u}_z\frac{\partial \tilde{u}_y}{\partial \tilde{z}}\right) = \nu\frac{V}{D^2}\frac{\partial^2 \tilde{u}_y}{\partial \tilde{y}^2} + \nu\frac{V}{L_c^2}\frac{\partial^2 \tilde{u}_y}{\partial \tilde{z}^2}$$

$$\left(\frac{W}{\tau}\frac{\partial \tilde{u}_z}{\partial \tilde{t}} + \frac{VW}{D}\tilde{u}_y\frac{\partial \tilde{u}_z}{\partial \tilde{y}} + \frac{W^2}{L_c}\tilde{u}_z\frac{\partial \tilde{u}_z}{\partial \tilde{z}}\right) = \nu\frac{W}{D^2}\frac{\partial^2 \tilde{u}_z}{\partial \tilde{y}^2} + \nu\frac{W}{L_c^2}\frac{\partial^2 \tilde{u}_z}{\partial \tilde{z}^2}.$$

54

Also substituting the scaling into the continuity equation, Eq.2.8 yields,

$$\frac{V}{D}\frac{\partial u_y}{\partial y} + \frac{W}{L_c}\frac{\partial u_z}{\partial z} = 0, \tag{2.9}$$

then the vertical velocity scales as $W \sim \frac{VL_c}{D}$. This results in two separate scalings,

$$Re_{L_c} = \frac{VL_c}{\nu_0} \text{ and } a = \frac{L_c}{D},$$

the Reynolds number and an aspect ratio respectively. The upper bounds of the length of the biofilm vary experimentally from $\sim 1\,\text{mm}$, for partially detached streamers in microfluidic channels, to $10\,\text{cm}$ in pipes, again within the boundary layer where the flow goes to $1 \times 10^{-3}\,\text{m} \cdot \text{s}^{-1}$. The maximum biofilm thickness is about $60\,\mu\text{m}$. The maximum biofilm thickness is flow and orientation dependent which should be studied in the future. Assuming that the viscosity and the density of the ensemble are that of the water, $Re_{L_c} < 0.01$ and the flow will always be laminar. Therefore the flow falls in the Stokes flow regime. The time dependent term remains to establish the boundary layer. Thus Eq. 2.7 becomes

$$\frac{\partial \mathbf{u}}{\partial t} = \nu \nabla^2 \mathbf{u} - \frac{1}{\rho}\nabla p - \frac{\nu}{k}\mathbf{u}. \tag{2.10}$$

The pressure is scaled by letting $p = \rho V^2 \tilde{p}$ and the permeability by letting $k = L_c D \tilde{k}$. James et al. and Tachie et al. did show the Brinkman model predicts a slip velocity that is 70% higher than the actual slip velocity but researches still find the Brinkman model computationally simpler and useful [29, 84, 55]. The experimentally determined permeability scales with porosity

$$k \simeq \frac{\phi^3}{(1-\phi)^2} \tag{2.11}$$

where ϕ is the porosity [52]. This scaling is taken to be equal for the first approximation. Substituting the scalings back in to Eq. 2.10 gives a dimensionless equation

$$\frac{\partial \tilde{u}_y}{\partial \tilde{t}} = \frac{Re_{L_c}^{-1}}{a}\left(a^2\frac{\partial^2 \tilde{u}_y}{\partial \tilde{y}^2} + \frac{\partial^2 \tilde{u}_y}{\partial \tilde{z}^2}\right) - \frac{\partial \tilde{p}}{\partial \tilde{y}} - Re_{L_c}^{-1}\frac{(1-\phi)^2}{\phi^3}\tilde{u}_y \qquad (2.12)$$

$$\frac{\partial \tilde{u}_z}{\partial \tilde{t}} = \frac{Re_{L_c}^{-1}}{a}\left(a^2\frac{\partial^2 \tilde{u}_z}{\partial \tilde{y}^2} + \frac{\partial^2 \tilde{u}_z}{\partial \tilde{z}^2}\right) - \frac{1}{a^2}\frac{\partial \tilde{p}}{\partial \tilde{z}} - Re_{L_c}^{-1}\frac{(1-\phi)^2}{\phi^3}\tilde{u}_y \qquad (2.13)$$

where the term on the left is the change in velocity over time, the first term on the right is the diffusion of momentum, the second term is the flow due to a pressure gradient and the last term is drag due to the porosity.

2.4.2   Solute Advection - Diffusion - Reaction

Since biofilms consume substrates, produce new chemicals from substrates, and produce waste products including ions, everything that obeys the following equations is a solute. A solute with concentration c will change with respect to time by flux into and out of the system and any creation or consumption of the substrate,

$$\frac{\partial(c\phi)}{\partial t} + \nabla \cdot \mathbf{N} = R, \qquad (2.14)$$

where ϕ is the porosity of the medium, $\mathbf{N}$ is the total flux, and R is the reaction rate. Multiple solutes may be coupled together through the reaction term or the flux term (binary diffusion). It is assumed that the viscosity and density of the fluid do not depend on concentration $\rho \neq \rho(c)$ and $\mu \neq \mu(c)$ which makes the flux terms almost linear.

The advective flux is the rate at which the solute is carried by the fluid and is given by

$$\mathbf{N}_{adv} = \mathbf{u}c, \qquad (2.15)$$

where $\mathbf{u}$ is the velocity of the bulk. The diffusive flux is the flux of the solute caused

by concentration gradients across the medium. The diffusive flux follows Fick's law,

$$\mathbf{N}_{diff} = -\mathbf{D}_d \nabla c, \tag{2.16}$$

where the Fickian diffusivity, D_d is related to the molecular diffusivity D_0. by the porosity and the tortuosity tensor $\mathbf{T}$ from [88]

$$\mathbf{D}_d = \frac{\phi}{T_y T_z} D_0 \begin{pmatrix} T_z & 0 \\ 0 & T_y \end{pmatrix}. \tag{2.17}$$

The dispersive flux is similarly

$$\mathbf{N}_{disp} = -\mathbf{D}_m \nabla c. \tag{2.18}$$

where mechanical diffusion (dispersion), $\mathbf{D}_m$, typically dominates the diffusivity. In porous media, longitudinal dispersion dominates transverse dispersion and the diffusion coefficient is a tensor:

$$\begin{aligned} \mathbf{D}_m &= \alpha_T |\mathbf{u}| \delta_{ij} + (\alpha_L - \alpha_T) \frac{u_i u_j}{|\mathbf{u}|} \\ &= \alpha_T |\mathbf{u}| \mathbf{1} + (\alpha_L - \alpha_T) \begin{pmatrix} \frac{u_x^2}{|\mathbf{u}|} & \frac{u_x u_y}{|\mathbf{u}|} \\ \frac{u_x u_y}{|\mathbf{u}|} & \frac{u_y^2}{|\mathbf{u}|} \end{pmatrix} \end{aligned}$$

where $\alpha_{L,T}$ is the longitudinal and transverse dispersivity respectively ($\alpha_T \sim 0.1\alpha_L$). In a microbial fuel cell, the flux of charged particles responds to the electric field between the electrodes and between the electrodes and the bacteria. It is proportional to the concentration, electric field vector $\mathbf{E}$, mobility u and sign of charge,

$$\mathbf{N}_e = \frac{z}{|z|} u c \mathbf{E} \tag{2.19}$$

This term will be ignored at first pass although it is significant in slow flow and high

57

electric field strength. The total flux is then

$$
\begin{aligned}
\mathbf{N} &= \mathbf{N}_{adv} + \mathbf{N}_{diff} + \mathbf{N}_{disp} \\
&= -\left(\mathbf{D}_d + \mathbf{D}_m\right)\nabla c + \mathbf{u}c.
\end{aligned} \tag{2.20}
$$

The reaction term follows Monod or Michaelis-Menten reaction kinetics

$$
R = -\frac{q_m X_f c}{K_m + c} \tag{2.21}
$$

where q_m is the maximum substrate utilization rate, X_f is the biofilm density, and K_m is the half-maximum concentration.

Combining the reaction and the flux term,

$$
\frac{\partial(\phi c)}{\partial t} = \nabla((\mathbf{D}_d + \mathbf{D}_m)\,\nabla c) + \mathbf{u}\nabla c - \frac{q_m X_f c}{K_m + c}. \tag{2.22}
$$

Since the velocity is already small, the mixed dispersion term, being second order, is negligible. The transverse dispersivity is already small, so it is also neglected. Even with these simplifications, the model remains coupled and sufficiently complex to capture some of the effects of the porosity on the flow and vice versa. Without going into more detail than is possible without discussing X_f and the relation $\phi = 1 - \frac{X_f}{\rho_f}$, let $c = c_0 x_s$ where x_s is the mole fraction, the s to distinguish it from the biomass. Let $K_m = c_0 \tilde{K}_m$, with the other scalings, $y, z, \mathbf{u}$ the same as the fluid flow,

$$
\begin{aligned}
\frac{\partial x_s}{\partial \tilde{t}} &= \frac{Pe^{-1}}{a}\left(a^2\frac{\partial^2 x_s}{\partial \tilde{y}^2} + \frac{\partial^2 x_s}{\partial \tilde{z}^2}\right) + \frac{Pe^{-1}}{a\phi}\left(a^2\frac{\partial \phi}{\partial \tilde{y}}\frac{\partial x_s}{\partial \tilde{y}} + \frac{\partial \phi}{\partial \tilde{z}}\frac{\partial x_s}{\partial \tilde{z}}\right) \\
&\quad - \frac{1}{\phi}\left(\tilde{u}_y\frac{\partial x_s}{\partial \tilde{y}} + \tilde{u}_z\frac{\partial x_s}{\partial \tilde{z}}\right) - Da_s^{-1}\frac{x_s}{\tilde{K}_m + x_s}\frac{1 - \phi}{\phi} - \frac{x_s}{\phi}\frac{\partial \phi}{\partial \tilde{t}}. \tag{2.23}
\end{aligned}
$$

The Péclet number be defined as usual, $Pe = \frac{L_c^2/D_0}{D/V}$ a ratio of diffusive time to advection time. Similarly, the Damkohler number for substrate is the ratio of substrate utilization time to advection time $Da_s = \frac{q_m \rho_f/c_0}{D/V}$. The tortuosity is then seen to be little more than a weighting for the lack of straightness and the porosity shows up as

a compressibility factor. As such, the solutions presented in the results section drop the second term.

2.4.3 Biofilm evolution

The biofilm density X_f is the mass of biofilm per total volume. Using concepts from soil mechanics, it is assumed that there is some representative density of the biomass and secreted EPS ρ_f. If A is the cross sectional area of the biofilm and $L_f(y)$ is the height of the biofilm , then the volume of the pores is the total volume minus the volume of the biofilm

$$V_p = V_T - V_f = AL_f - AL_f \frac{X_f}{\rho_f}$$

or the porosity by definition is

$$\phi = 1 - \frac{X_f}{\rho_f}. \tag{2.24}$$

Rittman described the growth of the biofilm, X_f as a function of time as

$$\frac{\partial X_f}{\partial t} = \frac{Y q_m X_f c}{K_m + c} - b_{det} X_f - b_{death} X_f, \tag{2.25}$$

where the first term on the right is the Michaelis-Menten(Monod) growth of bacteria on a given media, c, with a yield Y at a rate q_m and a half max concentration K_m, b_{det} is rate of detachment and b_{death} is the rate of biofilm death[73]. The model for detachment used here is taken from soil mechanics instead of using a constant, or an empirical relation between flow and detachment[72, 34, 10]. The difference in the fluidized and dry shear tensors, $\boldsymbol{\sigma} - \boldsymbol{\sigma}_o$, is related to the strain tensor $\boldsymbol{\varepsilon}$ by

$$\boldsymbol{\sigma} - \boldsymbol{\sigma}_o = \left(K - \frac{2}{3}G\right) tr\boldsymbol{\varepsilon}\mathbf{1} + 2G\boldsymbol{\varepsilon} - b(p - p_o)\mathbf{1} \tag{2.26}$$

for a porous medium where K, the bulk modulus, is the volume response to a change in pressure and G, the shear modulus, is the lengthwise response to shear stress. There may be differences between the wet and the dry measurements of these parameters,

but that is not addressed in this thesis. The strain is a function of the porosity since the only 'elongation' is due to increased pore pressure

$$(1 - \phi_o)tr\varepsilon = \phi - \phi_o \tag{2.27}$$

By combining the equation for axial strain with the stress balance,

$$\frac{\phi - \phi_0}{1 - \phi_0} = \frac{2b(p - p_0)}{K + \frac{4}{3}G}. \tag{2.28}$$

When the shear stress exceeds a critical value σ_c, the adhesion strength that has been measured for certain species of bacteria, the film will detach. A model like this can relate phenomena found by Stoodley et al. and Ohashi et al. to measurable quantities, like G, K, b and the dry film properties [58, 80]. Here, the detachment rate due to shear is modeled as

$$
\begin{aligned}
b_{det} &= \frac{1}{2}\nu_p\phi\dot{\gamma}_{yz} + \nu_p\phi\mathbf{u} \cdot \nabla \\
&= \frac{1}{2}\nu_p\phi\left(\frac{\partial u_z}{\partial y} + \frac{\partial u_y}{\partial z}\right) + \nu_p\phi\mathbf{u} \cdot \nabla,
\end{aligned} \tag{2.29}
$$

where ν_p is Poisson's ratio and $\dot{\gamma}_{yz}$ is the rate of shear in the yz direction. When the biofilm is more porous, the biofilm particles are sheared and carried away faster. When the biofilm is not a smooth surface, the gradient is large and the biofilm detaches faster. When the fluid shear is high, the biofilm is sheared away faster. Therefore, the biofilm growth is

$$\frac{\partial X_f}{\partial t} = \frac{Yq_mX_fc}{K_m + c} - \frac{1}{2}\nu_p\phi\left(\frac{\partial u_z}{\partial y} + \frac{\partial u_y}{\partial z}\right)X_f - \nu_p\phi\mathbf{u} \cdot \nabla X_f - b_{death}X_f, \tag{2.30}$$

or when scaled

$$\frac{1}{\phi}\frac{\partial \phi}{\partial \tilde{t}} = -Da_f^{-1}\frac{1 - \phi}{\phi}\frac{x_s}{\tilde{K}_m + x_s} + \frac{1}{2}\frac{\nu_p}{a}\left(a^2\frac{\partial \tilde{u}_z}{\partial \tilde{y}} + \frac{\partial \tilde{u}_y}{\partial \tilde{z}}\right)(1-\phi) - \nu_p\left(\tilde{u}_y\frac{\partial \phi}{\partial \tilde{y}} + \tilde{u}_z\frac{\partial \phi}{\partial \tilde{z}}\right) + Da_d^{-1}\frac{1 - \phi}{\phi},$$
$$\tag{2.31}$$

where the Damkohler number for the biofilm growth is $Da_f = \frac{1/Yq_m}{D/V}$ and the Damkohler number for biofilm decay is $Da_d = \frac{1/b_{death}}{D/V}$. In solving this system, the explicit shear term is dropped, the second term on the right, but not the implicit drag term, the 3rd term, for simplicity.

2.4.4 Bioelectrochemistry

As mentioned in Sec. 1.3, the laminar-flow microbial fuel cell is proposed as a direct measurement device for the study of biofilms. A direct electrical signal and *in situ* images of the biofilm can be used to determine how and why the biofilm responds to external stress the way it does. An electrical model is needed to interpret the results of the electrical signal. This will not be simulated in this work, but is presented for completeness.

The current density, $\mathbf{j}$, can be modeled as a function of concentration and potential using Butler - Volmer kinetics

$$\mathbf{j} = nF\left[k_r c_{an}(t)e^{(1-\alpha)\frac{\Delta\phi}{V_{th}}} - k_o c_{ca}(t)e^{-\alpha\frac{\Delta\phi}{V_{th}}}\right], \tag{2.32}$$

where the thermal voltage at 20°C is $V_{th} = 25.85\,\text{mV}$, k_r, k_o are the reaction rates of the reductant (ferricyanide) and the oxidant (acetate), and $\Delta\phi$ is the potential between the electrodes [23].

Isolating the current at the anode, a capacitance model has been developed

$$\mathbf{j} = nF\frac{kC_T\delta}{w}\left(\frac{1}{1+x_1} - \frac{1}{1+x_2}\right) \tag{2.33}$$

such that

$$x_i = \exp\left(\frac{E_i - E\circ'}{V_{th}}\right) \tag{2.34}$$

where $i = 1$ is the electron collector and $i = 2$ is the electron donor and C_T is the total concentration of cytochromes in the biofilm [83].

As a comparison the capacitance could also be modeled as

$$C_\phi = \frac{Q}{V_{th}} \frac{e^{\Delta E/V_{th}}}{\left(1 + e^{\Delta E/V_{th}}\right)^2} \tag{2.35}$$

where $Q = eC_T$.[48].

Either way, the flow of electrons between the electrodes would need to be balanced by a balance of charge in solution and following a Poisson equation at the electrodes

$$-\nabla \cdot (\varepsilon_E \nabla \phi) = \rho_e = F \sum z_i c_i. \tag{2.36}$$

2.4.5 Model Summary

In summary, the equations that are solved are:

The Navier-Stokes equations in $\hat{y}, \hat{z}$

$$\frac{\partial \mathbf{u}}{\partial t} = \nu \nabla^2 \mathbf{u} - \frac{1}{\rho} \nabla p - \frac{\nu}{k} \mathbf{u}, \tag{2.37}$$

subject to Dirichelet $\mathbf{u} = U\hat{y}$ and Neumann $\frac{\partial p}{\partial y} = 0$ boundary conditions at the inlet and outlet respectively and no penetration at the top and bottom of the channel.

The mass conservation equation including properties of the porous matrix and reactive biofilm,

$$\begin{aligned}
\frac{\partial x_s}{\partial \tilde{t}} &= \frac{Pe^{-1}}{a} \left(\frac{a^2}{T_y} \frac{\partial^2 x_s}{\partial \tilde{y}^2} + \frac{1}{T_z} \frac{\partial^2 x_s}{\partial \tilde{z}^2} \right) \\
&- \frac{1}{\phi} \left(\tilde{u}_y \frac{\partial x_s}{\partial \tilde{y}} + \tilde{u}_z \frac{\partial x_s}{\partial \tilde{z}} \right) - Da_s^{-1} \frac{x_s}{\tilde{K}_m + x_s} \frac{1-\phi}{\phi} - \frac{x_s}{\phi} \frac{\partial \phi}{\partial \tilde{t}}.
\end{aligned} \tag{2.38}$$

subject to a Dirichelet $c = c_0$ at the inlet and in the bulk and $c = 0$ initially.

$$\frac{1}{\phi} \frac{\partial \phi}{\partial \tilde{t}} = -Da_f^{-1} \frac{1-\phi}{\phi} \frac{x_s}{\tilde{K}_m + x_s} - \nu_p \left(\tilde{u}_y \frac{\partial \phi}{\partial \tilde{y}} + \tilde{u}_z \frac{\partial \phi}{\partial \tilde{z}} \right) + Da_d^{-1} \frac{1-\phi}{\phi}, \tag{2.39}$$

subject to a Dirichelet $c = c_0$ at the inlet and in the bulk and $X_f = 0$ initially.

The pore pressure in the biofilm must satisfy

$$\frac{\phi - \phi_0}{1 - \phi_0} = \frac{2b(p - p_0)}{K + \frac{4}{3}G}. \tag{2.40}$$

The unknowns in the system are c, X_f, and $\mathbf{u}$ in dimensional form or x_s, ϕ, and $\tilde{\mathbf{u}}$ dimensionless. The knowns in the system are summarized in Tables: 2.2, 2.3.

Table 2.2: The collection of parameters necessary for implementing the mathematical model for fluid flow, growth, and substrate utilization. Parameters marked with (-) are determined by the experimental setup. For this simulation, these are the same as the device described in Sec.2.2.

Name	Character	Units	Value	Reference
Diffusivity (OAc in Water)	D_0	[m$^2 \cdot$ s^{-1}]	1.089×10^{-9}	[25]
Substrate utilization rate	q_m	[(kgCODOAc) $\cdot$ (kgCODBiomass)$^{-1} \cdot$ s^{-1}]	1.574×10^{-4}	[63]
Yield coefficient	Y	[(kgCODBiomass) $\cdot$ (kgCODOAc)$^{-1}$]	2.43×10^{-1}	[63]
Half-maximum concentration	K_m	[(kgCODOAc) $\cdot$ m^{-3}]	9.98×10^{-2}	[66]
Monolayer biofilm density	ρ_f	[kgCODBiomass) $\cdot$ m^{-3}]	2.00×10^{2}	[61]
Viscosity of Water (25°C)	μ	[Pa $\cdot$ s]	8.90×10^{-4}	[25]
Density of Water (25°C)	ρ	[kg $\cdot$ m^{-3}]	9.98×10^{2}	[25]
Velocity of bulk	V_0	[m $\cdot$ s^{-1}]	3.30×10^{-2}	-
Concentration of OAc	c_0	[(kgCODOAc) $\cdot$ m^{-3}]	6.40×10^{-1}	-
Decay rate	d	[s^{-1}]	1.157×10^{-6}	[90]
Length of plate	D	[m]	2.0×10^{-2}	-
Young's Modulus	E	[Pa]	6.4×10^{1}	[65]
Poisson's Ratio	ν_p	[]	0.3	[65]
Adhesion strength	σ_t	[Pa]	0.4 - 1	[65]

Table 2.3: In this table, I summarize the dimensionless variable used in the model. The hydrodynamic relaxation time dominates all processes as expected. The growth rate is faster than the substrate utilization rate unlike most simulations since I am looking at a monolayer growth instead of discrete or continuous processes.

Name	Character	Expression	Value
Solvent Reynolds #	Re	$\frac{\rho VL}{\mu}$	1.8148
Péclet #	Pe	$\frac{VL}{D_o}$	1.666×10^3
Damkohler # for growth	Da_g	$\frac{Y_{qm}}{V/L}$	4.6875×10^{-4}
Damkohler # for substrate	Da_c	$\frac{q_m \rho_f/c_0}{V/L}$	6.0281×10^{-5}
Damkohler # for decay	Da_d	$\frac{d}{V/L}$	1.967×10^{-9}
Normalized half-maximum concentration	$\tilde{K}_m$	K_m/c_0	1.560×10^{-1}
Film reynolds #	Re	$\frac{\rho_f V_0 L}{\mu_f}$	8.90×10^{-4}
Inlet velocity	V_0	V_0/V_0	1
Mole fraction	c/c_0	1	6.40×10^{-1}
Aspect ratio	a	L_c/D	2.75×10^{-3}

THIS PAGE INTENTIONALLY LEFT BLANK

Chapter 3

Results & Discussion

The results of operating the laminar flow microbial fuel cell are discussed in this chapter. Results are presented of electrochemical impedance spectroscopy, potentiostatic controlled polarization, and continuous operation at a fixed load. Also scanning electron micrographs are shown of the biofilm growth from multiple regions of the electrode. Lastly, results of the biofilm growth model are presented at various shear rates.

A baseline electrochemical impedance spectrum under potentiostatic control (pEIS) was determined for the LF-MFC without bacteria (Reference 600, Gamry Instruments, Philadelphia,PA USA) (cf. Figure 3-1). The ohmic resistance of the system is the real intercept at $399.79\,\Omega$ of the plot of imaginary versus real impedance. This is substantially less than that found in an active large microbial fuel cell, typically on the order of 1 kΩ.The linear behavior indicates that the system is kinetically limited as expected without the bacteria catalyst. There is weak capacitive behavior (a semi-circular arc) as expected from the system without bacteria. The capacitance shown is likely due to the layers of pyrolytic graphite as shown in Figure 2-11. The fuel was run at $60\,\mu\mathrm{L}\cdot\mathrm{min}^{-1}$ from a syringe pump (PHD 2000, Harvard Bioscience, Holliston, MA, USA) . The anolyte was 10 mM sodium acetate in a pH 7.2 phosphate buffer solution. The catholyte was 40 mM Potassium Ferricyanide in the same buffer solution. The frequency range was from 0.1 Hz to 1 MHz.

The electrochemical impedance spectrum (EIS) of the system was then taken after
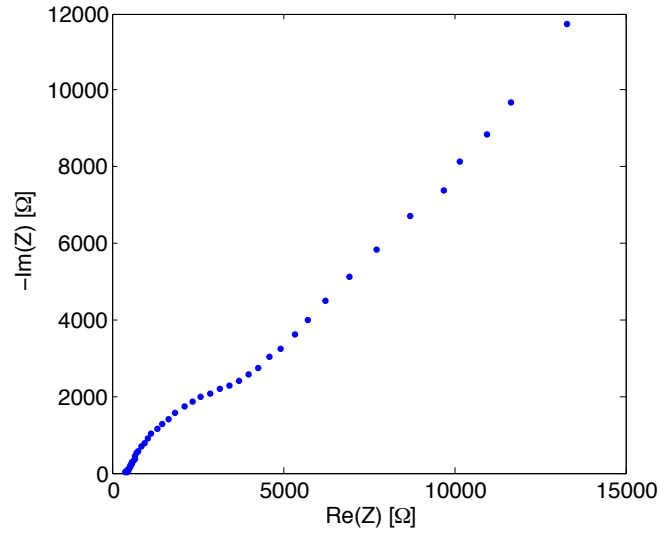
Figure 3-1: A baseline electrochemical impedance spectrum under potentiostatic control (pEIS) for the LF-MFC without bacteria. The ohmic resistance of the system is the real intercept at $399.79\,\Omega$ of the plot of imaginary versus real impedance. This is substantially less than that found in an active large microbial fuel cell, typically on the order of 1 kΩ.The linear behavior indicates that the system is kinetically limited as expected without the bacteria catalyst. There is weak capacitive behavior (a semi-circular arc) as expected from the system without bacteria. The capacitance shown is likely due to the layers of pyrolytic graphite as shown in Figure 2-11.
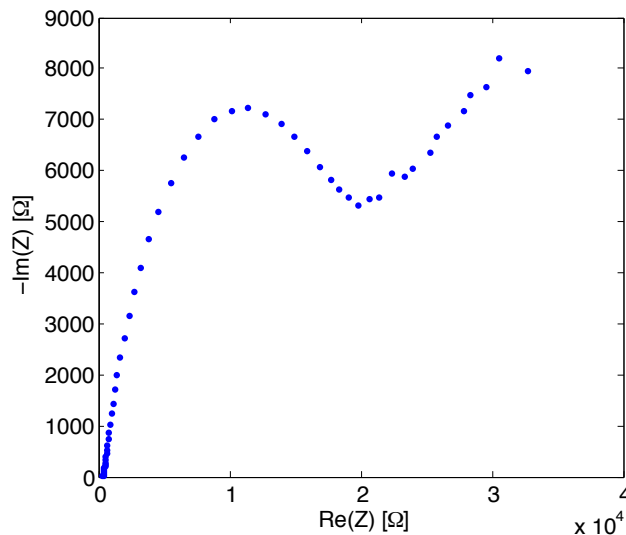
Figure 3-2: After 3 days of growth the electrochemical impedance spectroscopy of the system was taken the parameters identical to those in Figure 3-1. The internal resistance of the system is the intercept at $358.43\,\Omega$. The decrease in impedance in this fuel cell from the biofilm is likely due to the production of protons by the bacteria. The spectrum exhibits both mass transfer limitations and capacitance.

3 days of growth again under potentiostatic control (see Figure 3-2). The internal resistance of the system is the intercept at $358.43\,\Omega$. The decrease in ohmic resistance is likely due to the production of protons by the active biofilm. The spectrum exhibits both mass transfer limitations and capacitance. We can determine the nature of this full impedance circuit after further analytical modeling. The fuel was run at $120\,\mu L \cdot min^{-1}$ from a 100 mL fuel cell using a using gas flow from a nitrogen tank. The anolyte was 10 mM sodium acetate in a pH 7.2 phosphate buffer solution. The catholyte was 40 mM Potassium Ferricyanide in the same buffer solution. The frequency range of the AC current used in the EIS was from 0.1 Hz to 1 MHz.

After 3 days of growth, the polarization curve of the x-cell LF-MFC was obtained, Figure 3-3. The LF-MFC was left in open circuit for 24 hrs and the flow increased to show a higher OCV (as shown in Figure 3-4. The anolyte was 10 mM sodium acetate in a pH 7.2 phosphate buffer solution. The catholyte was 40 mM Potassium Ferricyanide in the same buffer solution. The data was taken using linear scan voltammetery at $0.1\,mV \cdot s^{-1}$ using a potentiostat (Reference 600, Gamry Instru-
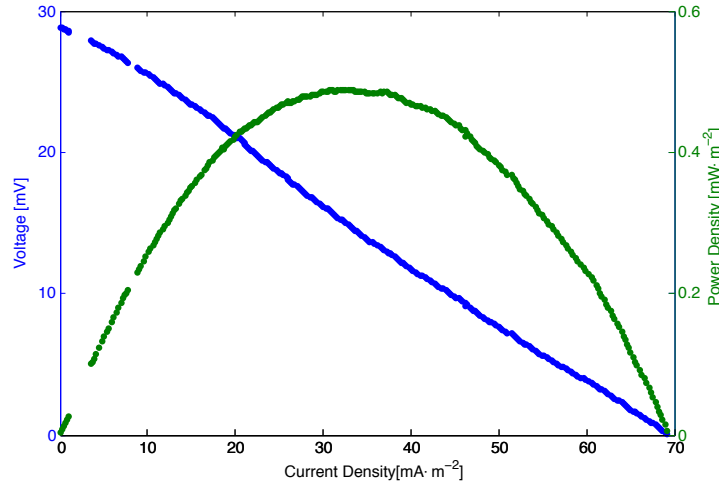
Figure 3-3: After 3 days of growth, the polarization curve of the x-cell LF-MFC was taken. The maximum power density was $\sim 0.4889\,\mathrm{mW} \cdot \mathrm{m}^2$. This is 3 orders less than the power density of the macro scale MFC. The open circuit voltage was $28.80\,\mathrm{mV}$ much less than the theoretical voltage of a MFC with acetate and ferricyanide ($\sim 700\,\mathrm{mV}$).

ments, Philadelphia,PA USA). The current and the power were normalized to the area of the anode, $7 \times 10^{-6}\,\mathrm{m}^2$. The maximum power density was $\sim 0.4889\,\mathrm{mW} \cdot \mathrm{m}^{-2}$. This is 3 orders of magnitude less than the power density of a macro scale MFC.

As indicated by the increase in voltage when the flow rate was increased in Figure 3-4, and the wide mass transfer control region in Figure 3-2, the low power may be due to mass transport limitation. One reason for this, noting that internal resistance was low and bacteria were present, could be that the system was being fed from an active fuel cell and the the acetate concentration could have been much lower than the original 10 mM. It may also be due to the high internal resistance. The simplest explanation might be the age of this cell versus the 3 month cell. The open circuit voltage was $28.80\,\mathrm{mV}$, much less than the theoretical voltage of an acetate | ferricyanide couple ($\sim 700\,\mathrm{mV}$). The LF-MFC was left in open circuit for 24 hrs and the flow increased to show a higher open circuit voltage (OCV), as shown in Figure 3-4. For comparison, after 3 months of growth, the polarization curve shown in Figure 3-5 of a 100 mL H-cell MFC was measured. The anolyte was 10 mM
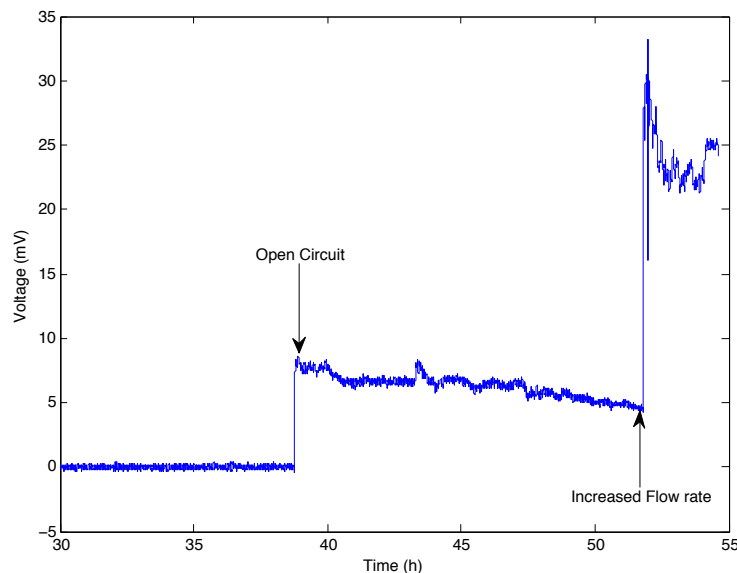
Figure 3-4: The voltage of the LF-MFC was monitored by connecting two leads across a $1\,k\Omega$ resistor connected to an AD converter. At this resistance the current and the voltage are too low to be distinguished from noise with the data acquisition system used (USB - 6008, National Instruments, UK). Using the data from the LSV at $1\,k\Omega$ the voltage is $\sim 0.4\,mV$ that is below the $1.5\,mV$ range of the device.

sodium acetate in a pH 7.2 phosphate buffer solution. The catholyte was 40 mM Potassium Ferricyanide in the same buffer solution. Each point in the curve was given 30 min to stabilize before obtaining a second data point (SourceMeter2400, Keithley Instruments, Cleveland, OH, USA). Again the current and the power were normalized with respect to the area of the electrode $592 \times 10^{-6}\,m^2$. The maximum power density was $\sim 200\,mW \cdot m^{-2}$. This MFC was later used to feed the LF-MFC.

The voltage of the LF-MFC was monitored by connecting two leads across a $1\,k\Omega$ resistor connected to an A-to-D converter (USB - 6008, National Instruments, UK) Figure 3-4. At this resistance the current and the voltage are too low to be distinguished from noise with the data acquisition system used. Using the data from the LSV, it was found that at $1\,k\Omega$ the cell voltage is $\sim 0.4\,mV$, This voltage is below the $1.5\,mV$ resolution of the A-to-D converter. Opening the circuit is standard practice before taking a linear scan voltammogram. The increase in flow rate was initially used to verify that the bacteria had formed a biofilm matrix [34], but was
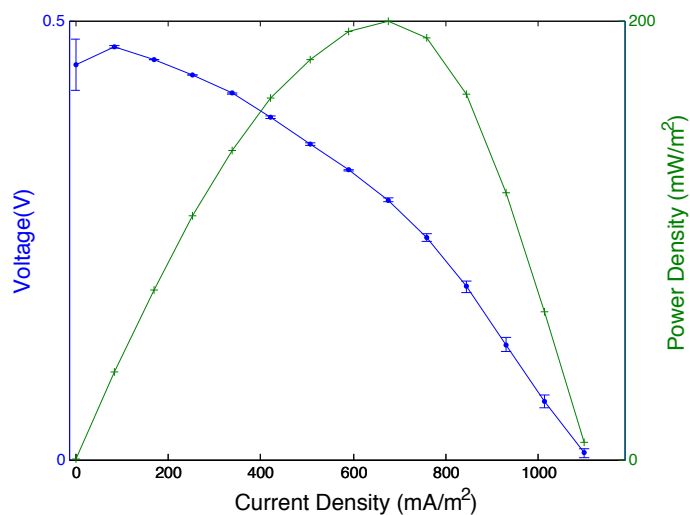
71

Figure 3-5: After 3 months of growth, the polarization curve of a 100 mL H-cell MFC was obtained. The anolyte was 10 mM sodium acetate in a pH 7.2 phosphate buffer solution. The catholyte was 40 mM Potassium Ferricyanide in the same buffer solution. Each point in the curve was given 30 min to stabilize before obtaining a second data point (SourceMeter2400, Keithley Instruments, Cleveland, OH, USA). The current and the power were normalized to the area of the electrode $592 \times 10^{-6} \, \mathrm{m^2}$. The maximum power density was $\sim 200 \, \mathrm{mW \cdot m^2}$. This MFC was later used to feed the LF-MFC.
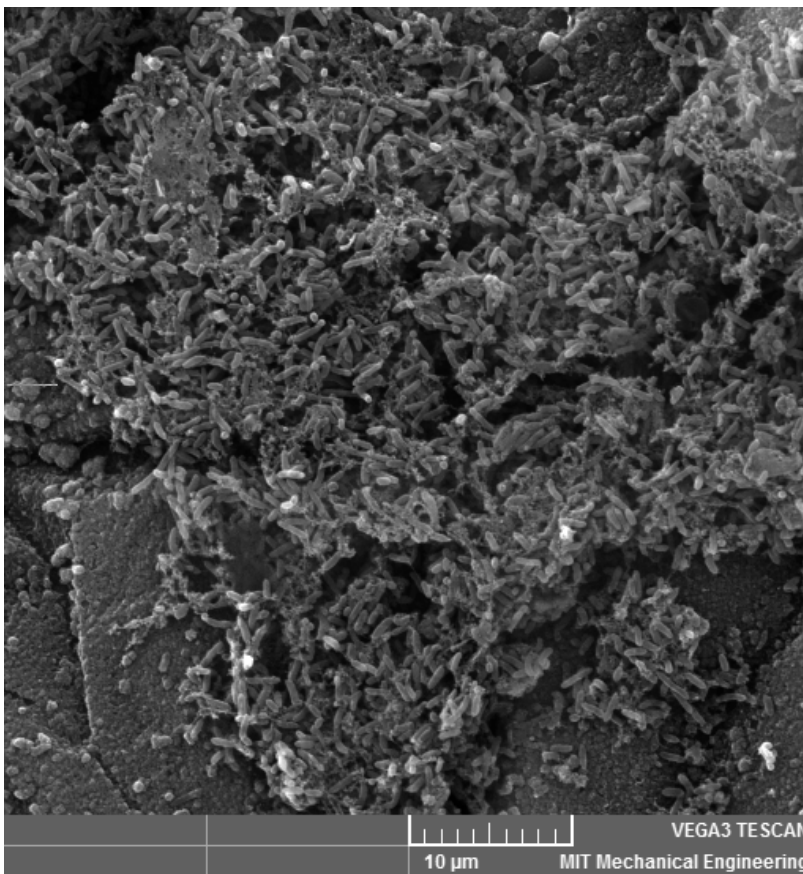
Figure 3-6: After 3 days of growth and operation, the LF-MFC was taken apart, the bottom half rinsed in buffer and then soaked in 4% glutaraldhyde solution (Sigma-Aldrich) to fix the bacteria. This was then dried in an ethanol series (30%, 50%, 75%, 100%) at 30 minutes each. The anode was then dried at the critical point of CO_2 to preserve the structure. This image was taken at 30 kV of a $40 \times 40\,\mu$m patch of the anode (Vega3, TESCAN - USA, PA, USA).

maintained after the OCV reached 30 mV. As mentioned above, the pEIS and LSV were also taken using this flow rate. The A-to-D converter was used because of its potential to measure multiple signals as compared with the Keithley SourceMeter and the Gamry Potentiostat. This would be necessary for any complete comparative study since the bacteria respond rapidly to any external stimulation and the stimulus duration.

Further confirmation that this current and voltage seen was due to a biofilm are found using scanning electron microscopy. The scanning electron micrograph shows a biofilm formed on the anode in Figure 3-6. This image was taken at 30 kV of a
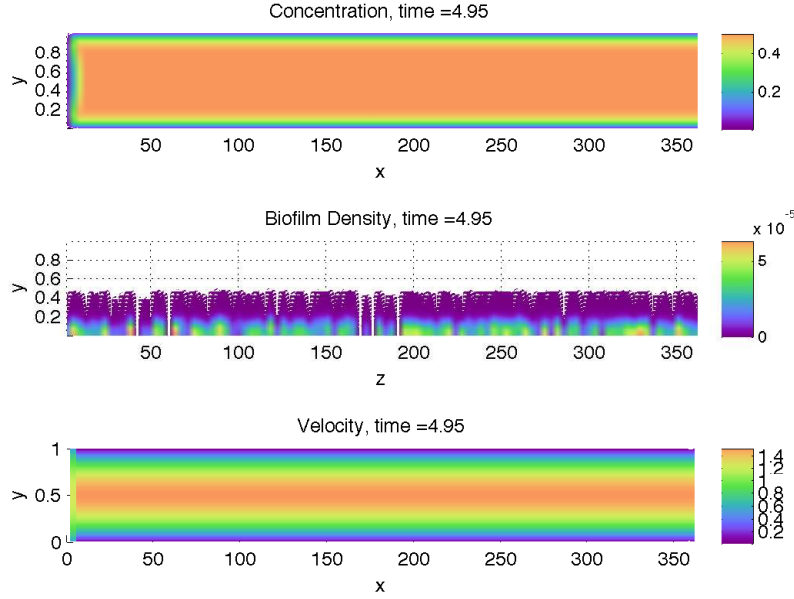
Figure 3-7: Substrate consumption biofilm growth, and fluid flow velocity from the LF-MFC model. The scheme runs in dimensionless and space. Normalizing length by the height of the channel $\tilde{D} = D/L_c = 363$. The mol fraction is 1 which is why there is no reaction based boundary layer. The Reynolds number is $Re^{-1} = 0$ shows the biofilm with "fluffy" characteristic as simulated by[13]. The biomass density plot in Figure 3-8 quantifies the absence of densification and agrees with their model.

$40 \times 40 \, \mu\text{m}$ patch of the anode.

The system of equations for substrate consumption, fluid flow, and biofilm growth was simulated in 2D using a finite volume implicit explicit MATLAB framework written by Uckerman & Lermusiaux (http://mseas.mit.edu/codes). It is a finite volume scheme, using total variational diminishing advection, and a pressure correction method to solve the transport equations. The original code was modified to include the biofilm as a 'tracer.' The Darcy permeability, substrate reaction, biofilm growth and death are handled explicitly. The scheme runs in dimensionless and space. The length was normalized by the height of the channel $\tilde{D} = D/L_c = 363$. The initial mole fraction of acetate is 1 which is why there is no reaction based boundary layer. Results are shown in Figure 3-7 where, $Re^{-1} = 0$ and the biofilm shows the "fluffy" characteristic as simulated by[13]. Under this no shear case, the biomass density plot in Figure 3-8 quantifies the absence of densification as predicted by the model
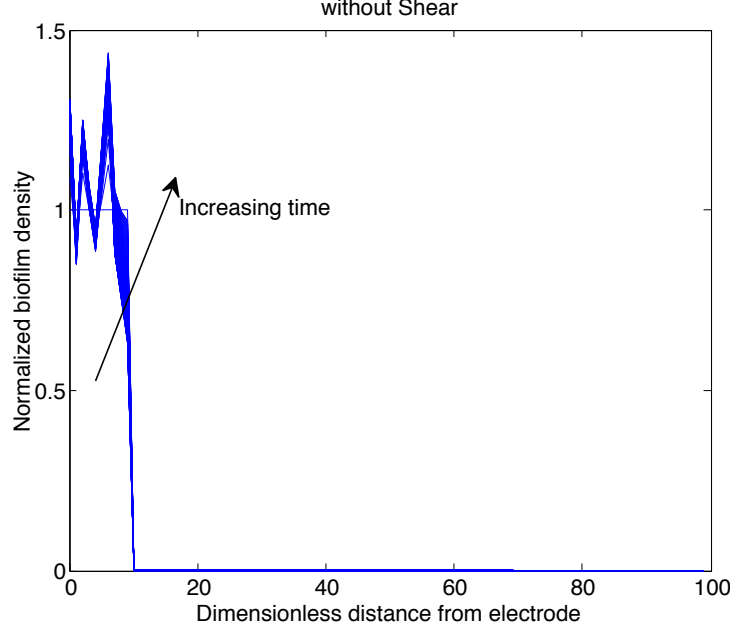
Figure 3-8: Biomass density versus height in a biofilm grown under no shear. The scheme runs in dimensionless and space. Normalizing length by the height of the channel $\tilde{D} = D/L_c = 363$. The mol fraction is 1 which is why there is no reaction based boundary layer. The Reynolds number is $Re^{-1} = 0$ and the biofilm has been normalized to its initial condition, flat line from 100-90 going up in height. Each line is a separate time step up to at $\tilde{t} = 5$. The figure does not show much deviation from 1 and shows biomass, though not appreciable, accumulating far into the channel at 30.

by Chambless et al. 2007 [13]. Chambless et al. does not provide data or model for separate cuts along the height of the biofilm, although their model could likely provide that data. The sum of biofilm mass at a given plane in height has been normalized with respect to its initial condition. Figure 3-8 shows multiple lines over time stopping at $\tilde{t} = 5$. The figure does not show much deviation from the initial normalized biomass density and shows biomass, though not appreciable, accumulating far into the channel at a dimensionless depth of 30. When the dimensionless viscosity is increased to $Re^{-1} = 2/3$ as shown in Figure 3-9 and the biofilm shows a short, compact characteristic as found experimentally by Stoodley et al. (cf. [81]). The biomass density plot in Figure 3-8 quantifies the absence of densification and agrees with their model. This figure shows large deviation from the initial conditions and
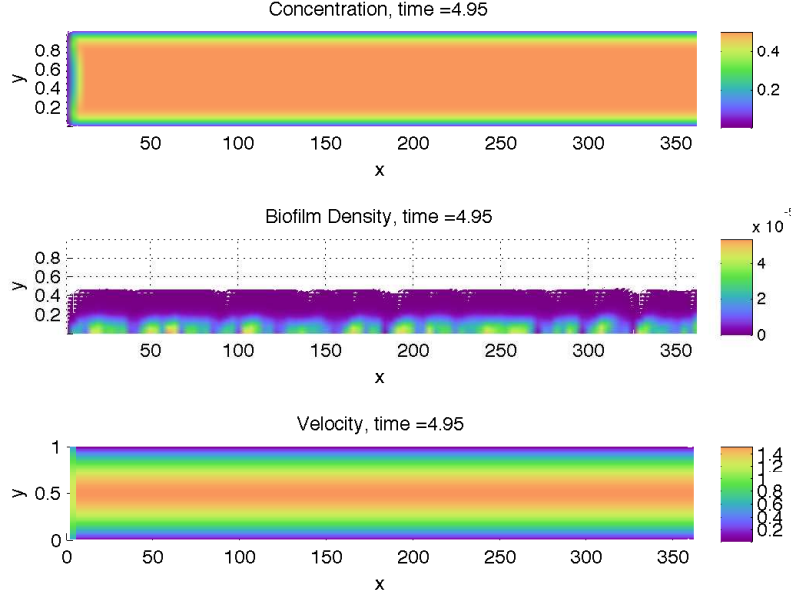
Figure 3-9: Simulation of substrate consumption, biofilm growth, and fluid flow with shear. The Reynolds number is $Re^{-1} = 2/3$ and the biofilm shows a short, compact characteristic as found by [81]. The biomass density plot in Figure 3-8 quantifies the absence of densification and agrees with their model.

shows minimal biomass growth into the channel. Additionally, there is biofilm loss between dimensionless depth 95 - 90 showing the biofilm is forced to reach a more dense equilibrium due to shear. While at first glance these images appear identical to the images of 2D biofilm growth by Picioreanu et al. they differ in that the biomass is not homogenous throughout [65]. There are gradients in biofilm porosity progressing down and across the biofilm, as experimentally found by [88]. It is this physically induced characteristic gradient that was the main push and contribution of this model.

These results were compared to the experimental results of Peyton [61]. The fit derived in that work was

$$X_f = K_r ho \sqrt{L_f} \qquad (3.1)$$

with R^2 values of 0.17 and 0.29 the data having very little correlation. The results here are best fit by exponential functions,

76
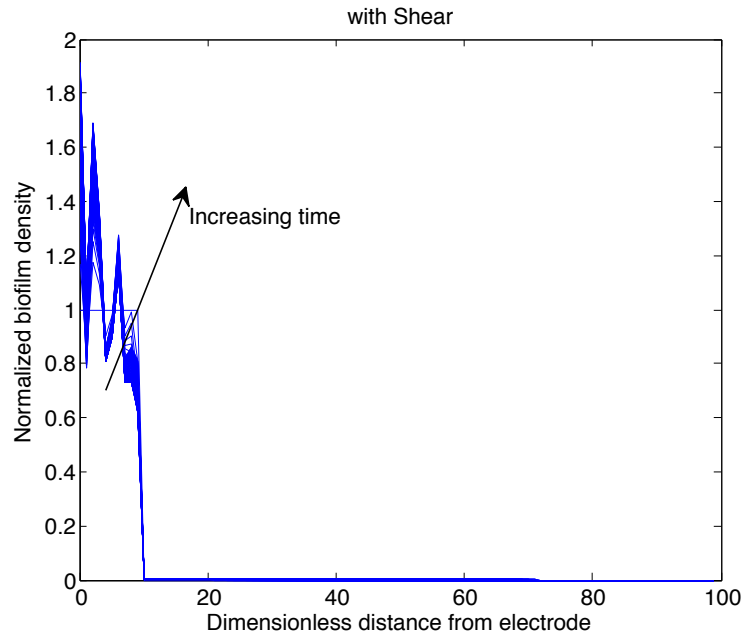
with Shear

Figure 3-10: Biomass density versus height with shear. There is a large deviation from the initial normalized value (1) and minimal biomass growth into the channel. Additionally, there is biofilm loss between 95 - 90 indicating that the biofilm is forced to reach a more dense equilibrium due to shear. The Reynolds number is $Re^{-1} = 2/3$ and the biofilm has been normalized to its initial condition, flat line from 100-90 going up in height. Each line is a time step and the simulation stops at $\tilde{t} = 5$.

Figure 3-11: A comparison of the normalized biofilm density versus distance from the growth surface (the electrode) when grown under shear and under no shear. A larger maximum density is found in the shear case in agreement with literature. From a mechanical perspective, this provides a larger binding area and hence greater adhesion strength it while maximizing substrate access. The rate at which the biofilm density decreases is increased for the case with shear, also as found in literature.
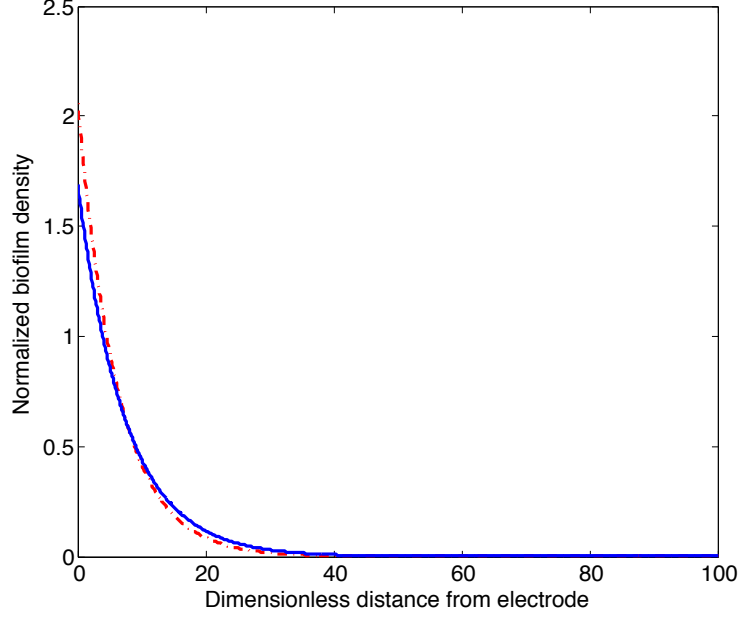
$$\frac{X_f}{X_f(0)} = K_\rho \exp\left(\frac{-aL_f}{L_c}\right), \tag{3.2}$$

with the maximum density $K_\rho = 2.061 \pm 0.185$ and $a = 0.1599 \pm 0.0096$ under shear and $K = 1.6913 \pm 0.0469$ and $a = 0.1346 \pm 0.0030$ without shear. Under shear, both K and a show the highest deviation after half the simulation time. Without shear, this deviation happens much later. The results here present an inverse curvature from that found by Peyton, likely due to the fact that the cells near the electrode are alive in this simulation as opposed those in Peyton.

Chapter 4

Conclusion & Future Work

Biofilms are communities of bacteria that respond dynamically to varying environmental stresses. A more complete understanding of biofilms will help us more efficiently grow them in microbial fuel cells or remove them from the human body. The tools that we have to study them are beginning to scale down from large reactors and beakers to length scales where we can see how biofilms' response at their time scale. The models of biofilm behavior and our ability to solve 3D coupled models are beginning to explain some of the phenomena surrounding the biofilms response to chemical stresses. We must now begin to look at how they respond to mechanical stresses with our new tools.

A new tool to study biofilms was developed in this thesis: a Laminar-Flow Microbial Fuel Cell (LF-MFC). Similarly a more complete model of biofilm growth under hydrodynamic control was developed. The device was designed to be compatible with conditions for biofilm growth and amenable to the use of light and confocal microscopy for direct measurement of the growing biofilm by using acrylic as the working material instead of other commonly used materials for microfluidcs, like poly(dimethyl siloxane). Machinist parameters were created to improve micro-machining not only for this device, but also other microfludic devices milled from acrylic.The device is more biocompatible than traditional lithographic electrodes and enables the use of more relevant materials by using solid-type electrodes. The 3-outlet design allows for more accurate indirect measurements of biofilm health including: substrate utiliza-

tion (chemical oxygen demand measurement), and pH change. The device is designed to measure total current and potential as a functional microbial fuel cell and another indirect measurement of biofilm health. The device tested with one type of electrode and one flow rate. Preliminary data is presented to guide further experiments on biofilm substrate compatibility, a biofilms response to shear, and the optimization of a microbial fuel cell.

A model has been developed that incorporates biofilm growth from a continuous perspective. The model constructed is not steady-state in either fluid flow or biofilm growth so that the evolution of all boundary layers, hydrodynamic, concentration, and biomass, can be observed. The biofilm's response to shear stress is explored where the biofilm is modeled as a poroelastic medium. Previous biofilm models (cf. Sec. 1.4) incorporated shear stress as a parametric constraint on external areas exposed to shear. Older models did not include flow through the biofilm, assuming it was negligible. The impact of shear stress in this model is only one part of the fluid flow that affects the porosity through the overall geometry and connectedness of the biofilm. Simulations at different shear rates tests not only reveal similar structure to previous models that included shear, but also begin to show some of the anisotropic structure that is characteristic of real world biofilms.

With the LF-MFC, future studies will be done to determine the impact of material chemistry on biofilm adhesion, formation and metabolism. This study will be guided by the free energy model mentioned in Sec. 2.2.3. The biofilms response to shear will be studied experimentally and numerically by varying the shear rate in the LF-MFC to test the hypothesis that a biofilm is a dynamic poroelastic medium as used in the model.

Appendix A

Machinist Parameters for a Laminar Flow - Microbial Fuel Cell

Tool parameters and setup have been optimized to yield a smooth surface finish and preserve flow geometry. It is recommended that any machining of a microfluidic device with similar parameters be done with similar.

All mill paths were and G-code was generated using MasterCam X5. The tool paths chosen for the channels was a "2D pocket Dynamic Area Mill." This produced an optimal path for hugging corners. A stepover of 5% diameter was used to minimize scalloping. Scalloping can also be reduced by using a finish pass. Since the depth of cut for this part is $55\,\mu$m, any finish pass would produce nanometer sized chips that could not be properly cleared with flood coolant. Atomized coolant is recommended for clearing the small chips in micro-machining to improve surface finish, minimize tool wear and part temperature the latter that can cause welding of chips to the part [31]. The mill used here is not equipped for that but the measured surface finish is at ~ 100 nm which is acceptable. Optimization of the cutting parameters matched the formula found by Vogler et al,

$$R_a \propto \frac{CL^2}{0.5D}$$

with a proportionality constant of 5 for acrylic [89].The path for the conductive tape,

electrical connectors was a parallel spiral without overlap since surface finish did not matter and a single spring pass of $10\,\mu$m. The spring pass is necessary for the pockets and kept for consistency. The pockets were similarly milled using a parallel spiral pass without overlap in one pass to a depth of $100\mu m$ for the carbon tape.

All parts were cut on a Microlution 363-S (Microlution, Chicago, IL, USA). This mill is equipped with a 56,000 rpm, air-turbine spindle with a 3.175 mm (1/8") dia chuck, flood coolant and air coolant. The pallet working area is $60 \times 58\,\mathrm{mm}(x \times y)$ and a custom fixture was made to hold each part in place to preserve alignment. The rotational velocity was limited to 48,000 rpm to minimize wear on spindle bearings. The channels were cut using a 0.254 mm (0.01") 4 flute end mill. This was chosen over smaller end mills and 2 flute end mills to minimize scalloping. The chip load was $1.9\,\mu$/tooth which gave a feed rate of $365\,\mathrm{mm/min}$.

Bibliography

[1] USGS Minerals Information: Commodity Statistics and Information. minerals.usgs.gov.

[2] Water and Sustainability: U.S. Electricity Consumption for Water Supply & Treatment -The Next Half Century. Technical Report 1006787, Palo Alto, CA, February 2002.

[3] Methacrylic Ester Polymers. In Herman F Mark, editor, Encyclopedia of Polymer Science and Technology, pages 1–29. John Wiley & Sons, April 2010.

[4] Folusho F Ajayi and Peter Weigele. A terracotta bio-battery. Bioresource Technology, 116:86–91, 2012.

[5] Jan Arends and Willy Verstraete. 100 years of microbial electricity production: three concepts for the future. Microbial Biotechnology, 5(3):333–346, 2012.

[6] Jerome T Babauta, Hung Nguyen, Timothy Harrington, Ryan Renslow, and Haluk Beyenal. pH, redox potential and local biofilm potential microenvironments within Geobacter sulfurreducens biofilms and their roles in electron transfer. Biotechnology and Bioengineering, 109(10):2651–2662, 2012.

[7] Jordan F Betz, Yi Cheng, Chen-Yu Tsao, Amin Zargar, Hsuan-Chen Wu, Xiaolong Luo, Gregory F Payne, William E Bentley, and Gary W Rubloff. Optically clear alginate hydrogels for spatially controlled cell entrapment and culture at microfluidic electrode surfaces. Lab on a Chip, 13(10):1854, 2013.

[8] Axel Blau, Tanja Neumann, Christiane Ziegler, and Fabio Benfenati. Replica-moulded polydimethylsiloxane culture vessel lids attenuate osmotic drift in long-term cell cultures. Journal of Bioscience, 34(1), March 2009.

[9] Anna K Boardman, Sandra Allison, Andre Sharon, and Alexis F Sauer-Budge. Comparison of anti-fouling surface coatings for applications in bacteremia diagnostics. Analytical Methods, 5(1):273–280, 2013.

[10] M Bouteca and J-P Sarda. Elements of thermoporoelasticity. In Philippe Charlez, editor, Mechanics of Porous Media, pages 21–58. A. A. Balkema Publishers, Rotterdam, May 1995.

[11] James D Bryers. Medical biofilms. Biotechnology and Bioengineering, 100(1):1–18, 2008.

[12] H J Busscher, A H Weerkamp, Henny C van der Mei, Antoon W J van Pelt, Hans P de Jong, and Joop Arends. Measurement of the surface free energy of bacterial cell surfaces and its relevance for adhesion. Applied and Environmental Microbiology, 48(5):980–983, 1984.

[13] Jason D Chambless and Philip S Stewart. A three-dimensional computer model analysis of three hypothetical biofilm detachment mechanisms. Biotechnology and Bioengineering, 97(6):1573–1584, August 2007.

[14] H Ted Chang and Bruce E Rittmann. Mathematical modeling of biofilm on activated carbon. Environmental Science and Technology, 21(3):273–280, March 1987.

[15] William G Characklis, Michael Trulear, J D Bryers, and N Zelver. Dynamics of biofilm processes: methods. Water Research, 16(7):1207–1216, January 1982.

[16] Gang Chen, Amy Chan-Hilton, and Mitch Williams. Modeling Bacterial Adhesion and Transport in the Environment: Surface Free Energy Relationships in Interpreting Bacterial Deposition in Porous Media. In Terri A Camesano and Charlene M Mello, editors, ACS Symposium Series, pages 245–260. American Chemical Society, Washington, DC, May 2008.

[17] Robert T Dehoff. Thermodynamics in Materials Science. CRC Press / Taylor & Francis, Boca Raton, FL, 2 edition, 2006.

[18] Ravindra Duddu, David L Chopp, and Brian Moran. A two-dimensional continuum model of biofilm growth incorporating fluid flow and shear stress based detachment. Biotechnology and Bioengineering, 103(1):92–104, May 2009.

[19] Herman Eberl, Eberhard Morgenroth, Daniel Noguera, Cristian Picioreanu, Bruce E Rittmann, Mark C M van Loosdrecht, and Oskar Wanner. Mathematical Modeling of Biofilms. Technical Report 18, London, UK, 2006.

[20] Dennis Enning, Hendrik Venzlaff, Julia Garrelfs, Hang T Dinh, Volker Meyer, Karl Mayrhofer, Achim W Hassel, Martin Stratmann, and Friedrich Widdel. Marine sulfate-reducing bacteria cause serious corrosion of iron under electroconductive biogenic mineral crust. Environmental Microbiology, 14(7):1772–1787, May 2012.

[21] Sergey V Ermakov, Stephen C Jacobson, and J Micahel Ramsey. Computer Simulations of Electrokinetic Transport in Microfabricated Channel Structures . Analytical Chemistry, 70(21):4494–4504, October 1998.

[22] C C Ezeuko, A Sen, A Grigoryan, and I D Gates. Pore-network modeling of biofilm evolution in porous media. Biotechnology and Bioengineering, 108(10):2413–2423, May 2011.

[23] Hubertus VM Hamelers, Annemiek ter Heijne, Nienke Stein, Rene A Rozendal, and Cees JN Buisman. Butler-Volmer-Monod model for describing bio-anode polarization curves. Bioresource Technology, 102(1):381–387, 2011.

[24] Mark J Hammer, Jr and Mark J Hammer. Water and Wastewater Technology. Pearson Prentice Hall, Upper Saddle River, N. J., January 2012.

[25] W M Haynes, editor. CRC Handbook of Chemistry and Physics. CRC Press / Taylor & Francis, Boca Raton, FL, 93 edition, April 2013.

[26] Z He, Shelley Minteer, and Largus T Angenent. Electricity generation from artificial wastewater using an upflow microbial fuel cell. Environmental Science and Technology, 39(14):5262–5267, 2005.

[27] Ellis I Hormats and Fred C Unterleitner. Measurement of the Diffusion of Oxygen in Polymers by Phosphorescent Quenching. The Journal of Physical Chemistry, 69(11):3677, November 1965.

[28] Geelsu Hwang, Chang-Ha Lee, Ik-Sung Ahn, and Byung Jin Mhin. Determination of reliable Lewis acid–base surface tension components of a solid in LW–AB approach. Journal of Industrial and Engineering Chemistry, 17(1):125–129, January 2011.

[29] David F James and Anthony M J Davis. Flow at the interface of a model fibrous porous medium. Journal of Fluid Mechanics, 426:47–72, 2001.

[30] Ranga S Jayashree, L Gancs, Eric R Choban, A Primak, Dilip Natarajan, Larry J Markoski, and Paul J A Kenis. Air-breathing laminar flow-based microfluidic fuel cell. Journal of the American Chemical Society, 127(48):16758–16759, 2005.

[31] Martin B G Jun, Suhas S Joshi, Richard E DeVor, and Shiv G Kapoor. An Experimental Evaluation of an Atomization-Based Cutting Fluid Application System for Micromachining. Journal of Manufacturing Science and Engineering, 130(3):031118–031118–8, 2008.

[32] Paul J A Kenis, Rustem F Ismagilov, and George M Whitesides. Microfabrication inside capillaries using multiphase laminar flow patterning. Science, 285(5424):83, 1999.

[33] Jeongyun Kim, Manjunath Hegde, Sun Kim, Thomas Wood, and Arul Jayaraman. A microfluidic device for high throughput bacterial biofilm studies. Lab on a Chip, 12(6):1157–1163, 2012.

[34] Junghyun Kim, Han-Shin Kim, Sewoon Han, Ji-Yun Lee, Jae-Eung Oh, Seok Chung, and Hee-Deung Park. Hydrodynamic effects on bacterial biofilm development in a microfluidic environment. Lab on a Chip, 13(10):1846, 2013.

[35] Erik Kjeang, Raphaelle Michel, David A Harrington, Nedjib Djilali, and David Sinton. A Microfluidic Fuel Cell with Flow-Through Porous Electrodes. Journal of the American Chemical Society, 130(12):4000–4006, 2008.

[36] Erik Kjeang, Brenton T Proctor, Alexandre G Brolo, David A Harrington, Nedjib Djilali, and David Sinton. High-performance microfluidic vanadium redox fuel cell. Electrochimica Acta, 52(15):4942–4946, 2007.

[37] Staffan Kjelleberg and Soeren Molin. Is there a role for quorum sensing signals in bacterial biofilms? Current opinion in microbiology, 5:254–258, May 2002.

[38] R Monina Klvens, Jonathan R Edwards, Chesley L Richards, Jr, Teresa C Horan, Robert P Gaynes, Daniel A Pollock, and Denise M Cardo. Estimating Health Care-Associated Infections and Deaths in U.S. Hospitals, 2002. Public Health Reports, 122(2):160, April 2007.

[39] W K Kwok, Cristian Picioreanu, S L Ong, M C M van Loosdrecht, W J Ng, and J J Heijnen. Influence of biomass production and detachment forces on biofilm structures in a biofilm airlift suspension reactor. Biotechnology and Bioengineering, 58(4):400–407, 1998.

[40] Raymond H W Lam, Min-Cheol Kim, and Todd A Thorsen. Culturing Aerobic and Anaerobic Bacteria and Mammalian Cells with a Microfluidic Differential Oxygenator. Analytical Chemistry, 81(14):5918–5924, 2009.

[41] Hyung-Sool Lee, César I Torres, Prathap Parameswaran, and Bruce E Rittmann. Fate of H2 in an Upflow Single-Chamber Microbial Electrolysis Cell Using a Metal-Catalyst-Free Cathode. Environmental Science and Technology, 43(20):7971–7976, January 2012.

[42] J G Leid, Mark E Shirtliff, J W Costerton, and Paul Stoodley. Human Leukocytes Adhere to, Penetrate, and Respond to Staphylococcus aureus Biofilms. Infection and Immunity, 70(11):6339–6345, November 2002.

[43] Jeff G Leid, Carey J Willson, Mark E Shirtliff, Daniel J Hassett, Matthew R Parsek, and Alyssa K Jeffers. The exopolysaccharide alginate protects Pseudomonas aeruginosa biofilm bacteria from IFN-gamma-mediated macrophage killing. Journal of immunology (Baltimore, Md. : 1950), 175(11):7512–7518, December 2005.

[44] G Lettinga, A F M van Velsen, S W Hobwa, W de Zeeuw, and A Klapwijk. Use of the upflow sludge blanket (USB) reactor concept for biological wastewater treatment, especially for anaerobic treatment. Biotechnology and Bioengineering, 22(4):699–734, 1980.

[45] Zhiqiang Li, Ying Zhang, Philip LeDuc, and Kelvin Gregory. Microbial electricity generation via microfluidic flow control. Biotechnology and Bioengineering, 108(9):2061–2069, 2011.

[46] Zhongjian Li, Arvind Venkataraman, Miriam A Rosenbaum, and Largus T Angenent. A Laminar-Flow Microfluidic Device for Quantitative Analysis of Microbial Electrochemical Activity. ChemSusChem, 5(6):1119–1123, June 2012.

[47] Bruce E Logan and John M Regan. Microbial Fuel Cells, Challenges and Applications. Environmental Science and Technology, 40(17):5172–5180, 2006.

[48] Nikhil S Malvankar, Tunde Mester, Mark T Tuominen, and Derek R Lovley. Supercapacitors Based on c-Type Cytochromes Using Conductive Nanostructured Networks of Living Bacteria. ChemPhysChem, 13(2):463–468, January 2012.

[49] Andrew Kato Marcus, César I Torres, and Bruce E Rittmann. Conduction-based modeling of the biofilm anode of a microbial fuel cell. Biotechnology and Bioengineering, 98(6):1171–1182, 2007.

[50] Andrew Kato Marcus, César I Torres, and Bruce E Rittmann. Analysis of a microbial electrochemical cell using the proton condition in biofilm (PCBIOFILM) model. Bioresource Technology, 102(1):253–262, 2011.

[51] J Cooper McDonald, David C Duffy, Janelle R Anderson, Daniel T Chiu, Hongkai Wu, Oliver J A Schueller, and George M Whitesides. Fabrication of microfluidic systems in poly(dimethylsiloxane). Electrophoresis, 21(1):27–40, 2000.

[52] Chester R McKee, Amar C Bumb, and Robert A Koenig. Stress-Dependent Permeability and Porosity of Coal. ROCKY MOUNTAIN ASSOCIATION OF GEOLOGISTS, pages 143–153, November 1988.

[53] J Monod. The growth of bacterial cultures. Annual Reviews in Microbiology, 3(1):371–394, 1949.

[54] Carey D Nadell, Joao de Bivar Xavier, and Kevin R Foster. The sociobiology of biofilms. FEMS microbiology reviews, 33(1):206–224, January 2009.

[55] Guillermo A Narsilio, Olivier Buzzi, Stephen Fityus, Tae Sup Yun, and David W Smith. Upscaling of Navier–Stokes equations in porous media: Theoretical, numerical and experimental approach. Computers and Geotechnics, 36(7):1200–1206, September 2009.

[56] United Nations. Millenium Development Goals Report 2010. United Nations Publications UNIDIR, June 2010.

[57] X Niu, S Peng, L Liu, W Wen, and P Sheng. Characterizing and patterning of PDMS-based conducting composites. Advanced Materials, 19(18):2682–2686, 2007.

[58] A Ohashi and H Harada. Adhesion Strength of Biofilm Developed in an Attached Growth Reactor. Water Science and Technology, 29(10):281–288, 1994.

[59] A Ohashi and H Harada. A novel concept for evaluation of biofilm adhesion strength by applying tensile force and shear force. Water Science and Technology, 34(5):201–211, 1996.

[60] Akiyoshi Ohashi, Takashi Koyama, Kazuaki Syutsubo, and Hideki Harada. A novel method for evaluation of biofilm tensile strength resisting erosion. Water Science and Technology, 39(7):261–268, 1999.

[61] Brent Peyton. Effects of shear stress and substrate loading rate on Pseudomonas aeruginosa biofilm thickness and density. Water Research, 30(1):29–36, 1996.

[62] Christian Pfeffer, Steffen Larsen, Jie Song, Mingdong Dong, Flemming Besenbacher, Rikke Louise Meyer, Kasper Urup Kjeldsen, Lars Schreiber, Yuri A Gorby, Mohamed Y El-Naggar, Kar Man Leung, Andreas Schramm, Nils Risgaard-Petersen, and Lars Peter Nielsen. Filamentous bacteria transport electrons over centimetre distances. Nature, 491(7423):218–221, October 2012.

[63] Cristian Picioreanu, Ian M Head, Krishna P Katuri, Mark C M van Loosdrecht, and Keith Scott. A computational model for biofilm-based microbial fuel cells. Water Research, 41(13):2921–2940, July 2007.

[64] Cristian Picioreanu, K P Katuri, I M Head, Mark C M van Loosdrecht, and K Scott. Mathematical model for microbial fuel cells with anodic biofilms and anaerobic digestion. Water Science and Technology, 2008.

[65] Cristian Picioreanu, Mark C M van Loosdrecht, and Joseph J Heijnen. Two-Dimensional Model of Biofilm Detachment Caused by Internal Stress from Liquid Flow. Biotechnology and Bioengineering, 72(2):205–218, 2001.

[66] Cristian Picioreanu, Mark C M van Loosdrecht, Thomas P Curtis, and Keith Scott. Model based evaluation of the effect of pH and electrode geometry on microbial fuel cell performance. Bioelectrochemistry, 78(1):8–24, April 2010.

[67] Cristian Picioreanu, Mark C M van Loosdrecht, and Joseph J Heijnen. A new combined differential-discrete cellular automaton approach for biofilm modeling: Application for growth in gel beads. Biotechnology and Bioengineering, 57(6):718–731, March 1998.

[68] Cristian Picioreanu, Mark C M van Loosdrecht, and Joseph J Heijnen. Effect of diffusive and convective substrate transport on biofilm structure formation: A two-dimensional modeling study. Biotechnology and Bioengineering, 69(5):504–515, September 2000.

[69] Michael C Potter. Electrical Effects Accompanying the Decomposition of Organic Compounds. Proceedings of the Royal Society of London. Series B, Containing Papers of a Biological Character, 84(571):260–276, 1911.

[70] Eugene W Rice, Rodger B Baird, Andrew D Eaton, and Lenore S Clesceri, editors. Standard Methods for Examination of Water and Wastewater 2012. American Public Health Association, Washington, DC, 22 edition, January 2012.

[71] Hanno Richter, Kevin McCarthy, Kelly P Nevin, Jessica P Johnson, Vincent M Rotello, and Derek R Lovley. Electricity Generation by Geobacter sulfurreducens Attached to Gold Electrodes. Langmuir, 24(8):4376–4379, 2008.

[72] Bruce E Rittmann. The effect of shear stress on biofilm loss rate. Biotechnology and Bioengineering, 24(2):501–506, 1982.

[73] Bruce E Rittmann and Jacques Manem. Development and experimental evaluation of a steady-state, multispecies biofilm model. Biotechnology and Bioengineering, 39(9):914–922, 1992.

[74] Bruce E Rittmann and Perry L McCarty. Model of steady-state-biofilm kinetics. Biotechnology and Bioengineering, 22(11):2343–2357, 1980.

[75] Roberto Rusconi, Sigolene Lecuyer, Nicolas Autrusson, Laura Guglielmini, and Howard A Stone. Secondary Flow as a Mechanism for the Formation of Biofilm Streamers. Biophysical Journal, 100(6):1392–1399, March 2011.

[76] Samuel K Sia and George M Whitesides. Microfluidic devices fabricated in poly (dimethylsiloxane) for biological studies. Electrophoresis, 24(21):3563–3576, 2003.

[77] Elodie Sollier, Coleman Murray, Pietro Maoddi, and Dino Di Carlo. Rapid prototyping polymers for microfluidic devices and high pressure injections. Lab on a Chip, 11(22):3752–3765, 2011.

[78] Howard A Stone and S Kim. Microfluidics: basic issues, applications, and challenges. AIChE Journal, 47(6):1250–1254, 2001.

[79] Paul Stoodley, John D Boyle, Dirk deBeer, and Hilary M Lappin-Scott. Evolving perspectives of biofilm structure. Biofouling, 14(1):75–90, June 1999.

[80] Paul Stoodley, Dirk deBeer, and Zbigniew Lewandowski. Liquid Flow in Biofilm Systems. Applied and Environmental Microbiology, 60(8):2711–2716, August 1994.

[81] Paul Stoodley, Zbigniew Lewandowski, John D Boyle, and Hilary M Lappin-Scott. Structural deformation of bacterial biofilms caused by short-term fluctuations in fluid shear: An in situ investigation of biofilm rheology. Biotechnology and Bioengineering, 65(1):83–92, 1999.

[82] Paul Stoodley, K Sauer, D G Davies, and J W Costerton. Biofilms as complex differentiated communities. Annual Review of Microbiology, 56(1):187–209, October 2002.

[83] Sarah Strycharz-Glaven, RM Snider, A Guiseppi-Elie, and Leonard M Tender. On the electrical conductivity of microbial nanowires and biofilms. Energy & Environmental Science, 4(11):4366–4379, 2011.

[84] Mark F Tachie, David F James, and Iain G Currie. Velocity measurements of a shear flow penetrating a porous medium. Journal of Fluid Mechanics, 493:319–343, 2003.

[85] Michael Trulear and William G Characklis. Dynamics of Biofilm Processes. Journal (Water Pollution Control Federation), 54(9):1288–1301, September 1982.

[86] Amin Valiei, Aloke Kumar, Partha P Mukherjee, Yang Liu, and Thomas Thundat. A web of streamers: biofilm formation in a porous microfluidic device. Lab on a Chip, 12(24):5133–5137, 2012.

[87] Wouter van der Star, Wiebe Abma, Dennis Blommers, Jan-Willem Mulder, Takaaki Tokutomi, Marc Strous, Cristian Picioreanu, and Mark van Loosdrecht. Startup of reactors for anoxic ammonium oxidation: Experiences from the first full-scale anammox reactor in Rotterdam. Water Research, 41(18):4149–4163, 2007.

[88] A S Van Wey, A L Cookson, T K Soboleva, N C Roy, W C McNabb, A Bridier, R Briandet, and P R Shorten. Anisotropic nutrient transport in three-dimensional single species bacterial biofilms. Biotechnology and Bioengineering, 109(5):1280–1292, December 2011.

[89] Michael P Vogler, Richard E DeVor, and Shiv G Kapoor. On the Modeling and Analysis of Machining Performance in Micro-Endmilling, Part I: Surface Generation. Journal of Manufacturing Science and Engineering, 126:685, November 2004.

[90] O Wanner and W Gujer. A multispecies biofilm model. Biotechnology and Bioengineering, 28(3):314–328, March 1986.

[91] Oskar Wanner and P Reichert. Mathematical modeling of mixed-culture biofilms. Biotechnology and Bioengineering, 49(2):172–184, 1996.

[92] Stephen Whitaker. Flow in porous media I: A theoretical derivation of Darcy's law. Transport in Porous Media, 1(1):3–25, 1986.

[93] Jinwei Zhang, Enren Zhang, Keith Scott, and J Grant Burgess. Enhanced Electricity Production by Use of Reconstituted Artificial Consortia of Estuarine Bacteria Grown as Biofilms. Environmental Science and Technology, 46(5):2984–2992, March 2012.